UC Santa Barbara

UC Santa Barbara Previously Published Works

Title

A joint inversion for shear velocity and anisotropy: the Woodlark Rift, Papua New Guinea

Permalink

https://escholarship.org/uc/item/3sj5n5sk

Journal

Geophysical Journal International, 206(2)

ISSN

0956-540X

Authors

Eilon, Zachary
Abers, Geoffrey A
Gaherty, James B

Publication Date

2016-08-01

DOI

10.1093/gji/ggw177

Peer reviewed

eScholarship.org Powered by the California Digital Library
University of California

Geophysical Journal International

Geophys. J. Int. (2016) **206,** 807–824
Advance Access publication 2016 May 1
GJI Seismology

doi: 10.1093/gji/ggw177

A joint inversion for shear velocity and anisotropy: the Woodlark Rift, Papua New Guinea

Zachary Eilon,[1] Geoffrey A. Abers[2,3] and James B. Gaherty[3]

[1] *Department of Earth and Environmental Sciences, Lamont-Doherty Earth Observatory of Columbia University, Palisades, NY* 10964*, USA. E-mail: zeilon@ldeo.columbia.edu*
[2] *Cornell University, Ithaca, NY* 14853*, USA*
[3] *Lamont-Doherty Earth Observatory of Columbia University, Palisades, NY* 10964*, USA*

Accepted 2016 April 28. Received 2016 April 1; in original form 2015 October 24

SUMMARY

Trade-offs between velocity and anisotropy heterogeneity complicate the interpretation of differential traveltime data and have the potential to bias isotropic tomographic models. By constructing a simple parametrisation to describe an elastic tensor with hexagonal symmetry, we find analytic solutions to the Christoffel equations in terms of fast and slow horizontal velocities that allow us to simultaneously invert differential traveltime data and splitting data from teleseismic *S* arrivals to recover 3-D velocity and anisotropy structure. This technique provides a constraint on the depth-extent of shallow anisotropy, otherwise absent from interpretations based on *SKS* splitting alone. This approach is well suited to the young Woodlark Rift, where previous studies have found strong velocity variation and substantial *SKS* splitting in a continental rift with relatively simple geometry. This study images a low-velocity rift axis with ≤4 per cent spreading-parallel anisotropy at 50–100 km depth that separates regions of pre-existing lithospheric fabric, indicating the synchronous development of extensional crystallographic preferred orientation and lithospheric thinning. A high-velocity slab fragment north of the rift axis is associated with strike-parallel anisotropic fast axes, similar to that seen in the shallow mantle of some subduction zones. In addition to the insights provided by the anisotropy structure, the improvement in fit to the differential traveltime data demonstrates the merit to a joint inversion that accounts for anisotropy.

Key words: Body waves; Seismic anisotropy; Seismic tomography; Continental tectonics: extensional; Dynamics of lithosphere and mantle.

1 INTRODUCTION

1.1 Background

Seismic anisotropy is a widespread feature of the uppermost mantle and, in many places, is strong enough to cause traveltime anomalies on the same order as isotropic velocity variations (Anderson 1989; Bezada *et al.* 2014). In addition to removing spurious velocity artefacts, a consideration of anisotropy has the potential to offer dynamic and structural insights by providing a proxy for time-integrated strain history and internal fabric. Yet most tomographic models neglect the effect of anisotropy because of the complexity it adds to the inverse problem and the inability of standard differential traveltime measurements to sufficiently resolve the additional parameters it requires. Here, we present a method for simplifying the anisotropic parametrisation and collecting data that is sensitive to anisotropy and velocity heterogeneity in order to invert jointly for velocity and anisotropy structure.

The complex elastic anisotropy of natural rocks and the nonlinearity of anisotropic effects mean that anisotropic body wave tomography poses a difficult problem. Teleseismic shear wave splitting studies image vertically integrated anisotropic structure with good horizontal resolution but they lack the ability to resolve more than one or, occasionally, two layers of anisotropy (Silver & Savage 1994), due to a paucity of data, near-vertical ray paths, lack of crossing rays and the non-commutativity of the splitting operator (Silver & Long 2011). By making simplifications to parametrise weak anisotropy (Thomsen 1986; Mensch & Rasolofosaon 1997), 3-D anisotropic traveltime inversions have been attempted (e.g. Pratt & Chapman 1992) but the problem is ill-conditioned and mostly limited to *P*-wave anisotropy, often in subduction settings (Zhao *et al.* 2015) and assuming hexagonal symmetry (Wang & Zhao 2013). Shear wave splitting tomography from local earthquake signals has been carried out in the well-illuminated mantle wedge of a subduction zone (Pozgay *et al.* 2007; Abt *et al.* 2009) but the method has not proved straightforward to generalise. Anisotropic tomography using the 'multichannel method' (Chevrot 2000), which measures

© The Authors 2016. Published by Oxford University Press on behalf of The Royal Astronomical Society.

Downloaded from http://gji.oxfordjournals.org/ at Columbia University on June 6, 2016

the commutatively additive *splitting intensity*, has been developed in theory (Favier & Chevrot 2003; Chevrot 2006) but the necessity for excellent backazimuthal coverage has limited its application in practice. Other workers have decomposed data based on polarisation perpendicular or parallel to expected fast azimuth to estimate the effect of anisotropy, including depth resolution (Hammond & Toomey 2003; Boyd *et al.* 2004); this idea is the foundation for the method we present.

Continental rifts manifest strong seismic velocity variations as crust thins, cold lithosphere breaks up, and hot, seismically slow asthenosphere replaces it. Several rifts have also been shown to contain measurable anisotropy, variously attributed to small-scale convective flow (Gao *et al.* 1997), aligned melt pockets (Kendall *et al.* 2005), large-scale deformation (Tommasi *et al.* 1999; Vauchez *et al.* 2000) or mantle flow (Montagner *et al.* 2007), organised melt along steep lithospheric gradients (Holtzman & Kendall 2010), pre-existing lithospheric fabric (Kendall *et al.* 2006), or a combination of the above (Hammond *et al.* 2014). *SKS* splitting in rifts, such as Rio Grande and the Main Ethiopian Rift (MER), is dominated by spreading-perpendicular fast axes (Gok *et al.* 2003; Kendall *et al.* 2005) in contrast to mid-ocean ridges, where models and observations indicate spreading-parallel fast axes where strain has been sufficient to establish crystallographic preferred orientation (CPO) of olivine (Wolfe & Solomon 1998; Blackman & Kendall 2002). Therefore, detailed imaging of anisotropy within continental rifts has the potential to discriminate between, and inform our understanding of, different modes and dynamics of extension (Vauchez *et al.* 2000).

1.2 Tectonic setting

The Woodlark Rift lies in a zone of broad oblique convergence between the Australian and Pacific plates, where a belt of microplates manifest complex tectonics including rapid rotation, translation, multiple recent subduction episodes and associated volcanism. The Woodlark is one of the youngest and most rapidly extending rifts known, with 70–190 km of opening (Taylor *et al.* 1999; Petersen & Buck 2015) since the late Miocene, and contains ultrahigh pressure (UHP) metamorphic rocks that ascended from their maximum P, T equilibration at $\geq$100 km depth since 5–8 Ma (Baldwin *et al.* 2008; Gordon *et al.* 2012). Lithospheric removal and consequent asthenospheric upwelling along the rift axis has given rise to strong velocity heterogeneities. Hot axial material is juxtaposed with a seismically fast and seismogenic body to the north of the rift that may be a relict slab, possibly related to UHP burial (Eilon *et al.* 2015). *SKS* measurements indicate strong anisotropy within this rift, with spreading-parallel fast axes that can be attributed to mantle CPO developed during extension (Eilon *et al.* 2014). However, without depth constraints on the anisotropy it is difficult to reconcile the tomographic images with *SKS* data, and to separate lithospheric from asthenospheric effects. The 2-D, orthogonal geometry and well-defined boundaries of this rift, together with the probability of trade-offs between isotropic velocity structure and strong anisotropy, make this an ideal proving ground for a joint velocity–anisotropy imaging study.

2 ANISOTROPIC PARAMETRISATION

A full description of anisotropic velocities within a model volume would involve too many free parameters for a tractable inverse problem; defining the anisotropic elastic tensors of natural rocks requires between 5 and 21 independent parameters per node. Although previous workers have implicitly assumed CPO by summing elastic tensors scaled to those for various known mineralogies to construct aggregate anisotropic tensors (Pozgay *et al.* 2007; Abt & Fischer 2008), the parametrisation established in this study is agnostic as to the mechanism of the anisotropy. It is not clear that the data are sufficiently good to warrant a more complex parametrisation, and the introduction of assumptions regarding mantle mineralogy and CPO would add unnecessary uncertainty. Instead, we describe the anisotropy and velocity within a model volume by the fewest possible parameters, by making a number of simplifying assumptions.

Consistent with natural and experimental petrofabrics of deformed olivine aggregates (Christensen 1984; Ismaïl & Mainprice 1998; Hansen *et al.* 2014), we assume an elastic tensor with hexagonal symmetry and horizontal symmetry axis; this geometry captures anisotropy imaged for horizontal CPO (Tommasi *et al.* 1999) or aligned melt pockets (Kendall *et al.* 2005). We link P and S velocities by assuming equal P and S anisotropy and fixing the ratio, ν, between average V_P and V_S. In this simple framework, a vertically incident shear wave would be split into two quasi-shear pulses, orthogonally polarised parallel to, and perpendicular to, the symmetry axis, with velocities $V_\parallel$ and $V_\perp$, respectively (Fig. 1). These are related to the two physically relevant parameters, average shear velocity, $V_{S_{\text{av}}}$, and fractional anisotropy, α, as follows:

$$\begin{aligned} V_\parallel &= V_{S_{\text{av}}}(1+\alpha) \\ V_\perp &= V_{S_{\text{av}}}(1-\alpha) \end{aligned} \tag{1}$$

so:

$$V_{S_{\text{av}}} = \frac{V_\parallel + V_\perp}{2} \qquad \alpha = \frac{V_\parallel - V_\perp}{V_\parallel + V_\perp}. \tag{2}$$

An arbitrarily incident shear wave will be split into two orthogonal pulses which may have different velocities. Because of the hexagonal symmetry, these velocities are purely a function of the angle (ζ) between the propagation direction and the symmetry axis (Fig. 2). Assuming that the value of the anisotropic parameter $\eta \approx 1$ in the upper mantle (Appendix A) (Anderson 1989; Tommasi *et al.* 2000), we can then show (eqs A2–A8) that the two velocities into which any shear wave will be split are:

$$\begin{aligned} V_{SH}(\zeta) &= \sqrt{V_\perp^2 \sin^2\zeta + V_\parallel^2 \cos^2\zeta} \\ V_{SV}(\zeta) &\approx \sqrt{V_\parallel^2 \cos^2 2\zeta + \left(\nu^2\left[V_\parallel^2 - V_\perp^2\right]/4 + V_\parallel^2\right)\sin^2 2\zeta} \end{aligned} \tag{3}$$

and

$$\cos\zeta = \sin i\,(\cos\theta\cos\phi + \sin\theta\sin\phi) \tag{4}$$

where i is the incidence angle measured from the vertical, θ is the ray propagation azimuth and ϕ is the azimuth of the symmetry axis (Fig. 1). In this context, V_{SV} denotes the shear velocity perpendicular to ray propagation that is in the plane containing the propagation vector and the hexagonal symmetry axis, and V_{SH} is the shear velocity perpendicular to this plane. In the case of vertical incidence, these reduce to $V_{SH} = V_\perp$ and $V_{SV} = V_\parallel$. The nomenclature comes from the common assumption of radial anisotropy ('transverse isotropy') where V_{SV} is *vertical* and V_{SH} is *horizontal* (e.g. Maupin & Park 2007).

By comparison to the solutions to the Christoffel equations, we show that the V_{SH} vector is always perpendicular to the symmetry axis, and that the V_{SV} vector is approximately parallel to the

Downloaded from http://gji.oxfordjournals.org/ at Columbia University on June 6, 2016

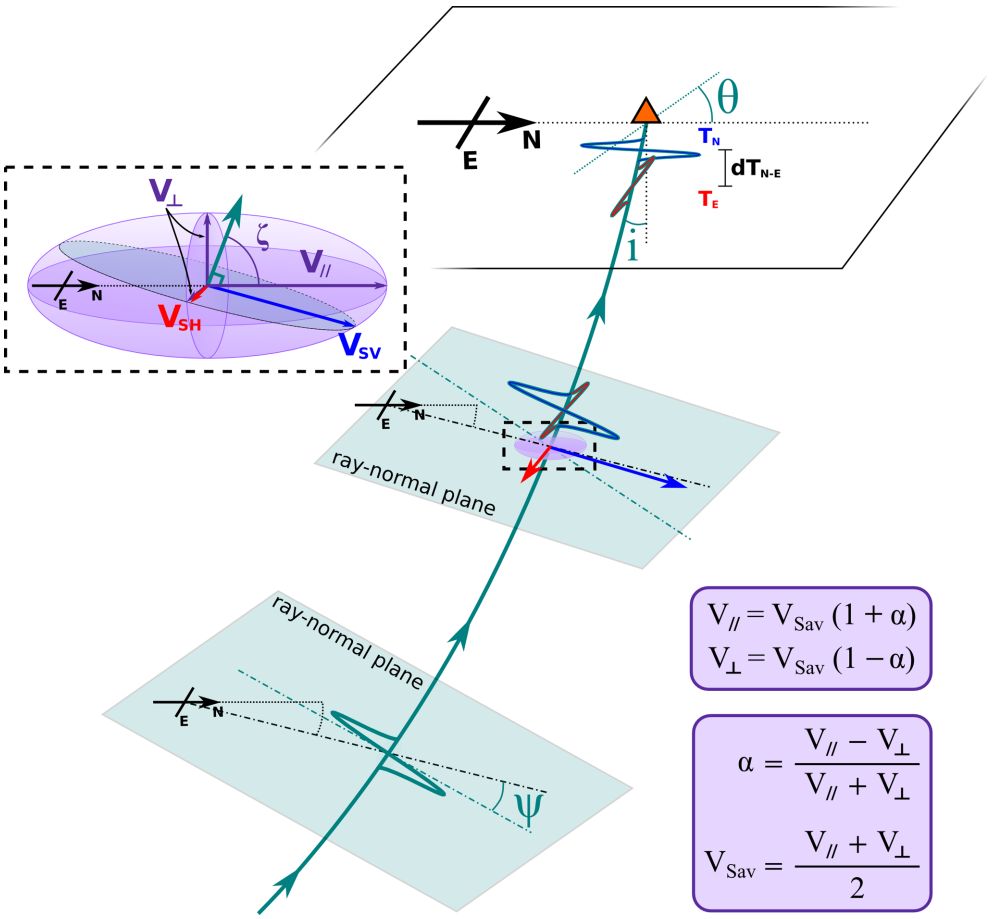

Figure 1. Schematic diagram of ray interacting with anisotropic structure, showing angles and velocities defined in the text.

symmetry axis for upper-mantle teleseisms ($\sim 47 \leq \zeta \leq 85^\circ$), reaching a maximum angular error of 22° for incidence angles relevant to our data (Fig. 2).

Finally, the E–W striking, N–S opening Woodlark Rift and the simple, predominantly N–S fast anisotropy measured here from *SK(K)S* splitting (Eilon *et al.* 2014) suggests a natural geometry for the anisotropic fabric in this particular setting. We therefore assume that the fabric is orientated such that the symmetry axis is oriented north–south. This fixes the permitted fast direction to N–S (for $\alpha > 0$ and $V_\perp < V_\parallel$) or E–W (for $\alpha < 0$ and $V_\perp > V_\parallel$). We have tested the choice of fixing the symmetry axis N–S versus E–W and found that this choice has a negligible effect on the result of the inversion. Using the notation, $u = \sin i \cos\theta = \cos\zeta$ (since $\phi = 0$), eq. (3) simplifies to:

$$V_{SH} = \sqrt{u^2 V_\parallel^2 + (1-u^2)\, V_\perp^2}$$

$$V_{SV} \approx \sqrt{V_\parallel^2 + v^2 u^2 (1-u^2)\left(V_\parallel^2 - V_\perp^2\right)} \qquad (5)$$

where V_{SV} is the velocity travelled at by waves polarised north–south and V_{SH} is the velocity of waves polarised east–west; these velocities determine relative timing of shear wave arrivals recorded on the N–S and E–W components of seismic instruments, respectively (Appendix B). Note that V_{SH} and V_{SV} are each sensitive to both $V_\perp$ and $V_\parallel$ for non-vertical incidence.

By making these assumptions, we have derived analytically differentiable expressions relating traveltimes of orthogonally polarised *S*-wave arrivals to anisotropy strength, polarity (N–S or E–W) and isotropic velocity variations. These expressions form the basis of an inverse problem for 3-D anisotropy and velocity structure. The parametrisation limits such an inversion to imaging N–S fast versus E–W fast anisotropy; azimuthal anisotropy with true fast azimuth intermediate to these directions will be projected onto this orthogonal basis, introducing artefacts and making our approach non-ideal for regions with more diverse or smoothly varying anisotropy. However, other orthogonal choices of symmetry axis azimuth can be easily accommodated by setting $\phi \neq 0$ in eq. (4).

3 DATA

Data were collected during the CDPapua passive seismic experiment, a 2010 March–2011 July deployment comprising 31 land-based broad-band PASSCAL seismometers and 8 broad-band OBS stations (Fig. 3a). The instruments were distributed on and around the D'Entrecasteaux Islands (DEI) over the ~250 × 250 km region of extended continent ahead of the propagating spreading centres, with station spacing of 20–50 km. Further details on instrumentation and deployment are described elsewhere (Eilon *et al.* 2014, 2015).

S-wave arrival times were measured for earthquakes $M_W \geq 5.5$ events between 30° and 90° from the array (as well as three events ≥90° with large diffracted phases): 335 earthquakes in all. For each arrival, a 200 s excerpt of data centred on the theoretical *S*-wave arrival (from IASP91) was detrended, tapered and padded with zeros, before being bandpass filtered. A hand-selected 20 s

Downloaded from http://gji.oxfordjournals.org/ at Columbia University on June 6, 2016

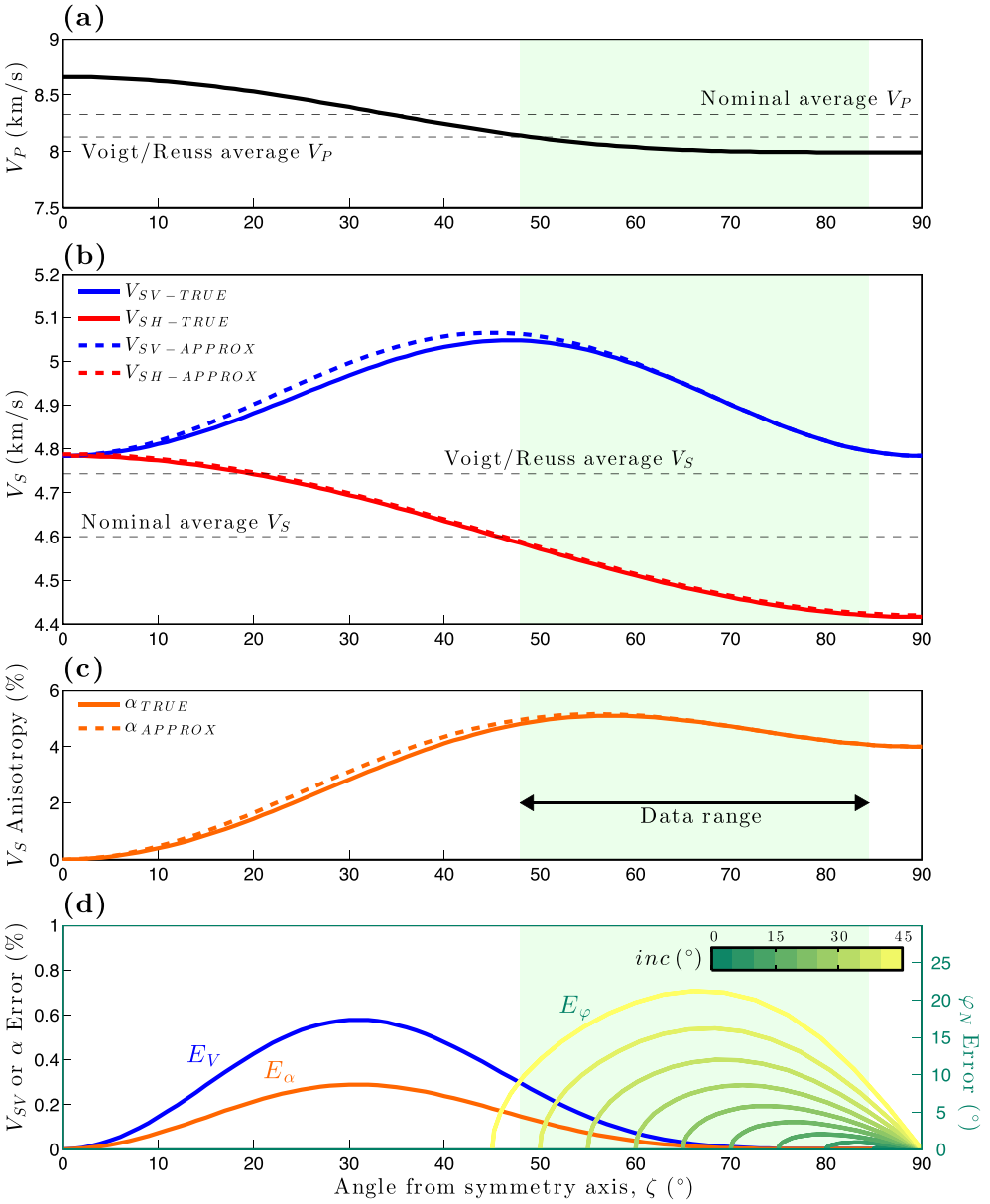

Figure 2. (a) *P*- and (b) *S*-wave velocity and (c) V_S anisotropy as a function of angle between the propagation vector and the symmetry axis for precise and approximate cases. (d) Error in V_{SV} and anisotropy (α) and difference between true fast azimuth and north for V_{SV}. The errors in polarisation and amplitude of anisotropy are computed as the difference between the solution to the Christoffel equations and the solutions to our simplified approximation to the anisotropy (eq. 5).

window of data around the predicted *S* arrival was excerpted for cross-correlation, applying a 20 per cent Tukey window. Only events with a distinct *S* phase were used.

For the purposes of investigating anisotropy, we measure both arrival time and polarisation, ψ, of arrival. For each event-station pair, the azimuth of the *S*-wave polarisation was measured using an eigenvalue approach (Vidale 1986), and averaged across all stations. Arrivals were classified by polarisation into octants: 'NS arrivals' having ψ within 22.5° of 0° (or 180°), 'EW arrivals' having ψ within 22.5° of ±90° and 'intermediate' arrivals, with ψ greater than 22.5° from any of the cardinal directions (Fig. 4). 'NS arrivals' travel through the model with velocity V_{SV} (eq. 5); for these events we measure station–station differential arrival times by cross-correlating waveforms measured on the north–south channel on our seismometers using the method of VanDecar & Crosson (1990) to measure δT_N. Correspondingly, 'EW arrivals' that travel at V_{SH} are measured on the east–west seismometer channels, giving δT_E. Tests indicate that the anisotropy does not change with depth sufficiently rapidly to cause twisting, whereby the polarisation changes along the ray path (Section 5.2).

'Intermediate arrivals' will be partitioned between the V_{SV} and V_{SH} principal directions, and will propagate along each with its respective velocity, accruing a time difference dT_{N-E} (the definition of shear wave splitting). As a result, arrivals at a given station measured on the NS and EW channels should have near-identical waveforms but arrive at different times. For these events we perform a three-way inversion, cross-correlating NS waveforms between all stations, cross-correlating EW waveforms between all stations and cross-correlating NS with EW waveforms at each station to compute splitting beneath that station. We adapt the least-squares approach

Downloaded from http://gji.oxfordjournals.org/ at Columbia University on June 6, 2016

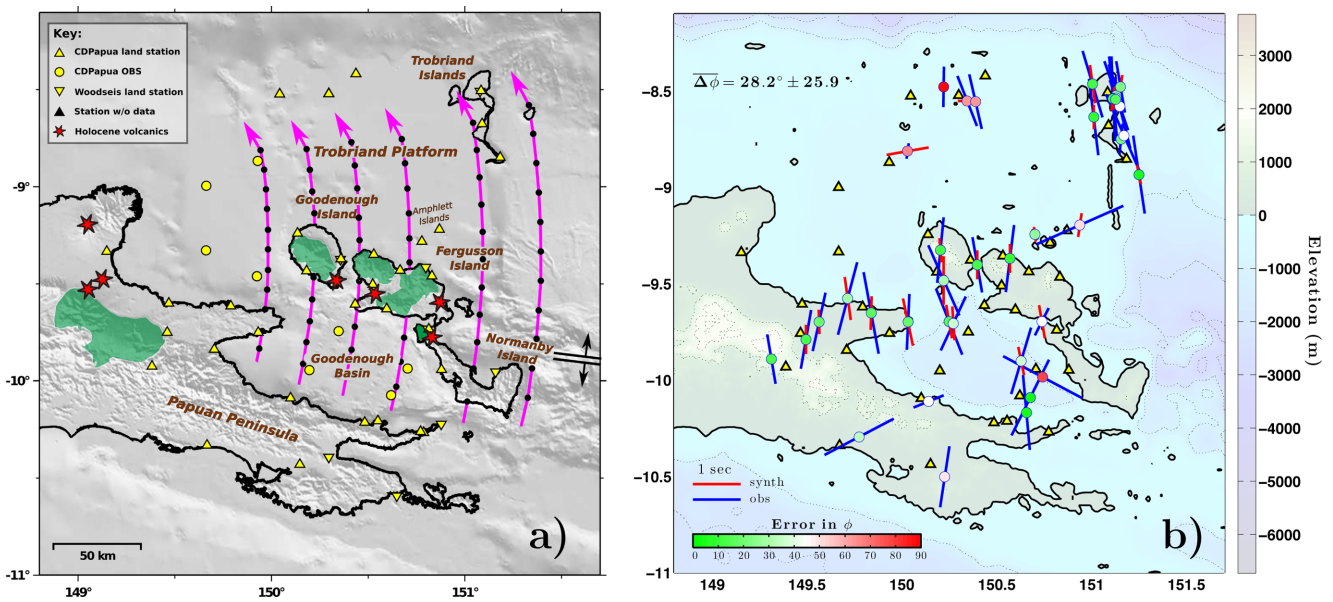

Figure 3. Maps of study area. (a) Deployment and geography, including station locations and types. Magenta lines: opening paths for Euler poles derived from seafloor magnetic anomalies to the east, with 0.5 Ma tick marks; along-strike extrapolation of western spreading centres also shown. (b) Results of synthetic splitting tests (Section 5.2) showing comparison between individual *SKS* observations (Eilon *et al.* 2014) and synthetic values obtained by propagating *SKS* waves through our final model structure. Only high-quality, non-null splitting observations were used. Best-fitting fast azimuth and splitting time are indicated by line orientation and length, respectively, and are plotted at 50 km depth piercing points. 1000 m elevation contours plotted.

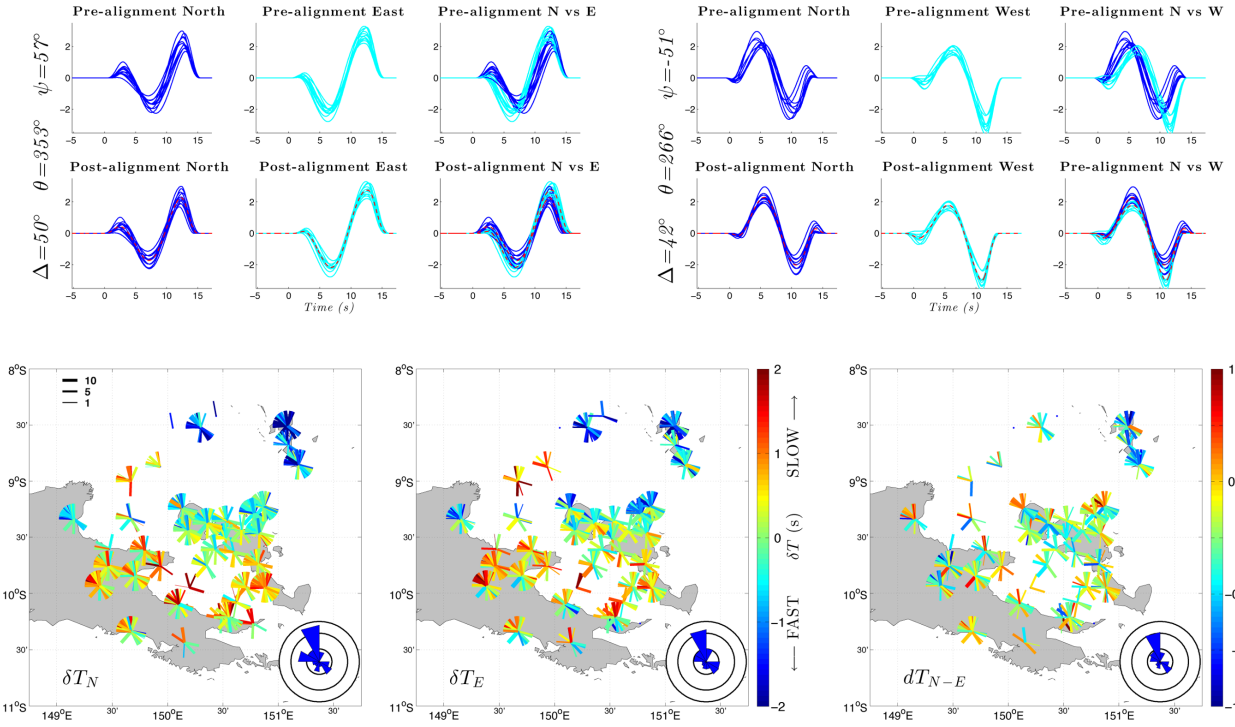

Figure 4. Top: examples of three-way cross-correlation (Appendix C) for an earthquake in Java sampling mostly N–S fast anisotropy (left) and an earthquake in Tohoku that carries a source-side signature of E–W fast anisotropy. Bottom: data used for this inversion, de-meaned to show only differential values of traveltime and splitting. Area-proportional rose diagrams indicate backazimuthal coverage, with concentric contours at 1000, 500 and 100 arrivals.

of VanDecar & Crosson (1990) to simultaneously invert for δT_E, δT_N and dT_{N-E} (Appendix C).

We emphasise that it is merely a convenient coincidence that the particular geometry of this rift is such that the anisotropic structure is aligned with cardinal seismometer components. The method we have presented here is general; if the geometry of the tectonics were different, a vertical-axis rotation would achieve the coordinate transformation required to measure arrivals on the appropriate orientations.

Filter frequencies were hand-selected for each set of arrivals to preserve as much high-frequency energy as possible while recovering a high-amplitude signal. The median corner frequencies were 0.125 and 0.02 Hz. Only arrivals with signal-to-noise ratio greater than 3 and with cross-correlation coefficient (c_{max}) greater than 0.7

Downloaded from http://gji.oxfordjournals.org/ at Columbia University on June 6, 2016

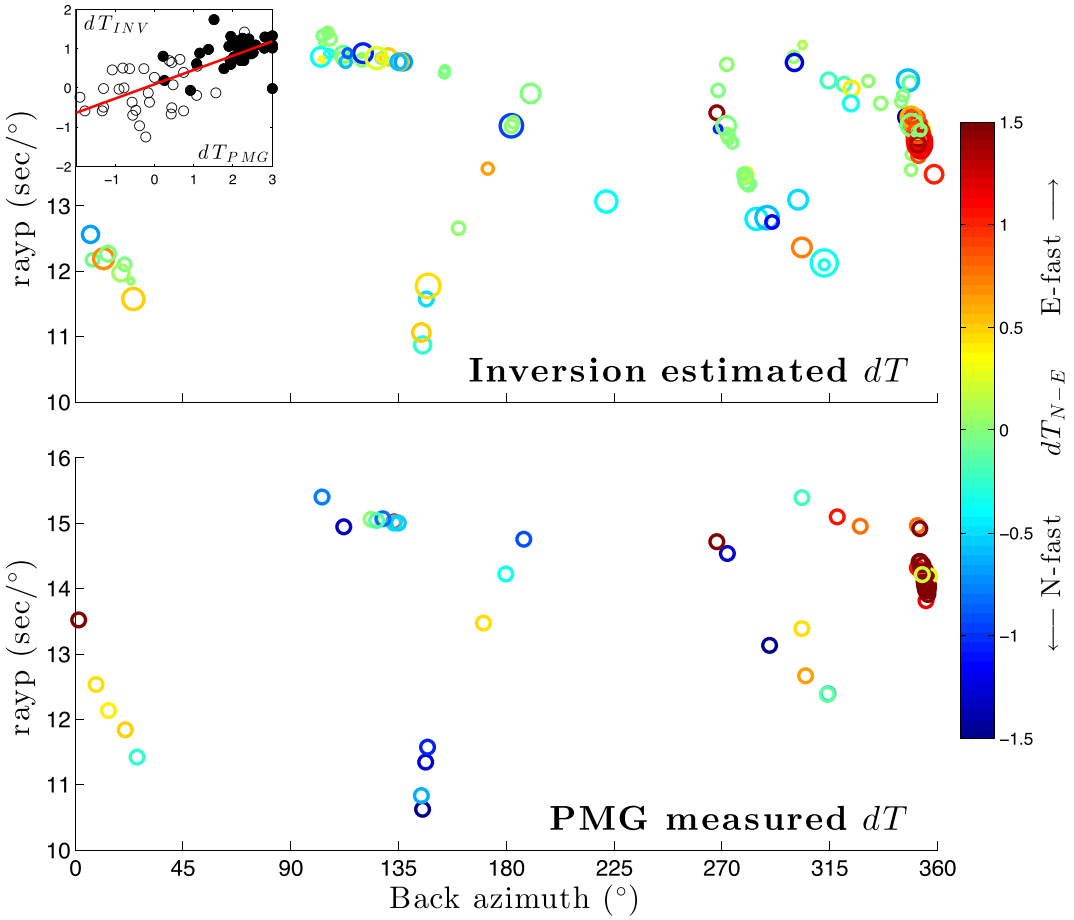

Figure 5. Source-side splitting terms (Section 3.1) estimated from the inversion (δT_{INV}: top) and measured at PMG (δT_{PMG}: bottom) plotted by mean backazimuth and ray parameter. The cluster of E-faster-than-N events from ∼350°N are Tohoku aftershocks. Inset: plot of δT_{PMG} versus δT_{INV} showing best-fit line with $R^2 = 0.54$, where filled symbols are from the Tohoku region.

were used. In order to avoid the δT values dominating the structure, we upweight the splitting measurements by the ratio of the number of δT_{N}: $dT_{\mathrm{N–E}}$ measurements (∼3).

3.1 Out-of-volume effects

Anisotropy measurements from direct *S* waves provide better depth resolution than core-traversing phases but may include splitting signal from anisotropy close to the source (Foley & Long 2011; Lynner & Long 2014) or in the mid-mantle (Fouch & Fischer 1996; Nowacki *et al.* 2015). The non-linearity and non-commutativity of anisotropic effects (Silver & Long 2011) make the problem of out-of-volume structure more complicated for splitting measurements than for differential teleseismic traveltimes. A good backazimuthal distribution and the inclusion of event $dT_{\mathrm{N–E}}$ terms serve to cancel out or capture the effects of anisotropy outside the model volume, respectively. Complex waveforms, identified by $<0.8\ c_{\max}$ between N–S and E–W arrivals, may have encountered multiple/complex splitting and are discarded. Station $dT_{\mathrm{N–E}}$ terms are included as model parameters in the inversion to account for anisotropy in the crust, although this term is damped to ensure that crustal splitting times are within the limits of what is generally observed (<0.5 s) (Yang *et al.* 2015).

As a check, $dT_{\mathrm{N–E}}$ values were measured directly from cross-correlation of north and east channels at the Port Moresby GSN station (PMG) 250 km to the west of the CDPapua array—this proximity means that teleseisms recorded at this station and recorded on our array have near-identical paths except in the upper mantle beneath the region. Null splitting measured from *SK(K)S* arrivals at PMG over a variety of backazimuths (Eilon *et al.* 2014) demonstrates that the upper mantle beneath this station is essentially isotropic. Therefore, any splitting of direct *S* waves measured at this station must arise from anisotropy close to the source or along the ray path, offering an independent estimate of out-of-volume splitting of waves impinging on the array.

There is a moderate correlation between the event $dT_{\mathrm{N–E}}$ terms solved for in the inversion and those measured at PMG ($R^2 = 0.54$). Plotting the $dT_{\mathrm{N–E}}$ terms by backazimuth and ray parameter (Fig. 5), there is a clear spatial agreement between the two data sets. In particular, there is a preponderance of ∼1.5 s positive (E faster than N) traveltimes from arrivals from the north (Japan) that are tightly grouped in backazimuth and ray parameter. This signal may arise from anisotropy in the region of the Marianas and Izu-Bonin slabs where Nowacki *et al.* (2015) and Lynner and Long (2015) record strong mid-mantle anisotropy. Importantly, the marked E-faster-than-N event terms from these earthquakes are in strong agreement with the PMG splitting measurements, demonstrating that this signal is attributable to source-side structure and can be removed.

Following this analysis, we use the $dT_{\mathrm{N–E}}$ values measured at PMG as *a priori* estimates of event splitting terms for the inversion, with moderate damping constraining deviation from these prior values.

Downloaded from http://gji.oxfordjournals.org/ at Columbia University on June 6, 2016

3.2 Traveltime residuals

In total, the data set comprises 1601 δT_{N} measurements, 1300 δT_{E} measurements and 969 $dT_{\mathrm{N–E}}$ measurements from 145 earthquakes. The rms residuals are 0.984, 1.340 and 1.167 s, respectively, and the demeaned values (removing the effect of mean splitting) are 0.984, 0.971, and 0.573 s. The similarity between de-meaned rms δT_{N} and δT_{E} implies that the majority of the differential traveltime signal is attributable to heterogeneities in average velocity. The ∼0.6 ratio between average $dT_{\mathrm{N–E}}$ and de-meaned rms differential traveltimes indicates that the magnitude of anisotropy heterogeneities is expected to be roughly 0.6 times that of velocity heterogeneities.

The measured differential arrival times (Fig. 4) on both components show traveltime delays in an E–W swath beneath the DEI, in agreement with isotropic tomography models (Eilon *et al.* 2015) that show the slow rift axis extending westwards from the seafloor spreading centre at ∼151.5°. Traveltime deficits seen at northern stations indicate a fast structure beneath the north of the array. Splitting data are noisier (and sparser) than differential traveltimes but show predominantly negative values (i.e. N–S arriving earlier than E–W) beneath the DEI.

4 TOMOGRAPHIC PROBLEM

4.1 Inversion approach

Following the approach of Schmandt & Humphreys (2010), we relate traveltime data to model parameters using finite-frequency velocity kernels with a first-fresnel zone approximation (also described in Eilon *et al.* 2015). Finite-frequency kernels for anisotropic media have been calculated (Favier & Chevrot 2003; Long *et al.* 2008) but by describing the model in terms of orthogonal velocities, the simpler velocity sensitivity kernels may be used. Our method also lends itself to incorporation of frequency-dependent splitting measurements (Long 2010) but that application is beyond the scope of this paper. The data include differential traveltimes, which are sensitive only to horizontal deviations in velocity and splitting times, which are also sensitive to absolute velocity. The anisotropic V_S model is defined on an irregular rectangular mesh with eight layers between 40 and 240 km depth (based on station spacing and array aperture) and horizontal node spacing increasing from 30 km at the centre to 40 km at the edge of the array. The nodes are parametrised in terms of absolute orthogonal velocities $V_\perp$ and $V_\parallel$, where the mean $V_{S_{\mathrm{av}}}$ at each depth is obtained from a local 1-D model for the top 40 km (Ferris *et al.* 2006) transitioning smoothly to the Voigt-averaged V_S from a global 1-D model (Kustowski *et al.* 2008) down to 400 km. We fix the V_P/V_S ratio, ν, equal to 1.81 (Ismaïl & Mainprice 1998) although this inversion, without *P*-wave data, is very weakly sensitive to this value. Tests varying ν between 1.6 and 2.0 yielded rms variations of just 0.03 per cent and 0.06 per cent in isotropic velocity perturbations and anisotropy, respectively, when compared to the preferred ν value. The model parameter vector then comprises nodal velocities, isotropic delays (δT) and splitting terms (dT) for each station and event: $\mathbf{m} = \{\mathbf{V}_\perp\,,\ \mathbf{V}_\parallel\,,\ \delta\mathbf{T}_{\mathrm{evt}}\,,\ \delta\mathbf{T}_{\mathrm{sta}}\,,\ \mathbf{dT}_{\mathrm{evt}}\,,\ \mathbf{dT}_{\mathrm{sta}}\}$.

The forward model, $\mathbf{g(m)}$, and Fréchet kernels, $\mathbf{G} = \partial\mathbf{g(m)}/\partial\mathbf{m}$, are themselves functions of the model parameters (Appendix B), so the inverse problem is non-linear and is solved iteratively by Newton's method with partial derivatives re-calculated at each iteration (Menke 2012, eq. 9.11):

$$\mathbf{m}_{k+1} = \mathbf{m}_k + \mathbf{G}_k^{-g}(\mathbf{d}_k - \mathbf{g}(\mathbf{m}_k)) \tag{6}$$

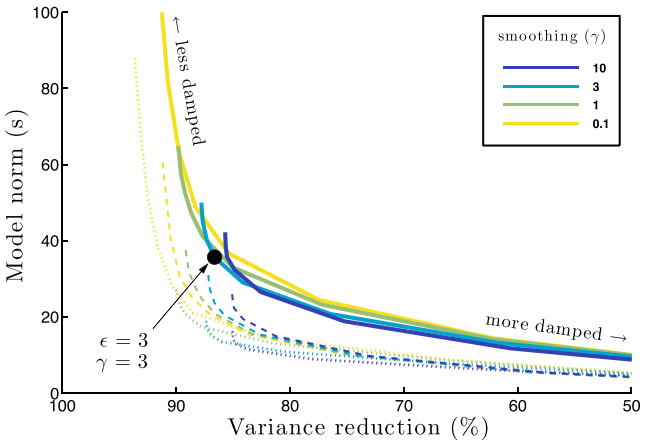

Figure 6. Results of 'L-tests' to ascertain the combination of regularisation parameters that mutually minimise misfit and model l^2-norm. Curves show results for values of damping (ϵ) between 0.3 and 30 and four different choices of smoothing. Dotted line: anisotropy model only ($dT_{\mathrm{N–E}}$ variance reduction versus α-norm); dashed line: velocity model only (δT variance reduction versus V-norm); solid line: total variance reduction versus total norm. For consistency of units, the V-norm and α-norms are calculated in seconds from the differential traveltime and splitting time, respectively, accrued by a vertical ray passing through each node. The preferred values of $\gamma = 3$ and $\epsilon = 3$ are indicated.

where $\mathbf{G}^{-g}$ denotes the 'generalised inverse', the solution to the weighted, damped least-squares problem that minimises the generalised error:

$$\Phi(\mathbf{m}) = \left|\left| \boldsymbol{\omega}^2(\mathbf{d}^{\mathrm{obs}} - \mathbf{g}(\mathbf{m})) \right|\right|^2 + \gamma\,||\,\mathbf{Lm}\,||^2 + \epsilon\,||\,\mathbf{m}\,||^2 \tag{7}$$

where $\boldsymbol{\omega}^2$ is a diagonal matrix of data weights ($= \boldsymbol{\sigma}_d^{-2}$) defined by $\sigma_i^{-1} = 0$ for $c_{\max} < 0.7$ and $\sigma_i^{-1} \propto 1 \rightarrow 2$ for $c_{\max}$ in the range $0.7 \rightarrow 1$. The constraints of first-derivative smoothing (imposed by $\mathbf{L}$) and damping are weighted by γ and ϵ, respectively (Menke & Eilon 2015). The solution is the least-squares solution to $\mathbf{Fm} = \mathbf{f}$, that is, $\mathbf{G}^{-g} = [\mathbf{F}^T\,\mathbf{F}]^{-1}\,\mathbf{F}^T$, where:

$$\mathbf{F}_k = \begin{bmatrix} \sigma_d^{-1}\,\mathbf{G}_k \\ \gamma\,\mathbf{L} \\ \epsilon\,\mathbf{I} \end{bmatrix} \quad \text{and} \quad \mathbf{f}_k = \begin{bmatrix} \sigma_d^{-1}\left(\mathbf{d} - \mathbf{g}(\mathbf{m}_k)\right) \\ \mathbf{0} \\ \mathbf{0} \end{bmatrix}. \tag{8}$$

The inversion is terminated after 20 iterations, or when the residual decreases by less than 1 per cent between iterations.

Regularisation of average velocity and anisotropy at a given node, i, is achieved by damping the values of $(V_\perp^i + V_\parallel^i)$ and $(V_\perp^i - V_\parallel^i)$, respectively. The ratio of vertical to horizontal smoothing is 0.4 and the sparser dT data require the anisotropy to be smoothed 3× more than velocity. Based on 'L-tests' (Fig. 6) that seek to mutually minimise model roughness and data misfit (Menke 1984), our preferred inversion uses $\gamma = 3$ and $\epsilon = 3$.

4.2 Resolution and squeezing

Resolution of the model is estimated by computing the hit quality [a combination of hit count and backazimuthal coverage; Eilon *et al.* (2015)] and the semblance [a quantitative measure of agreement between input and output checkerboard structures from synthetic tests; Zelt (1998)]. Regions expected to be well resolved have hit quality and semblance greater than 0.7; the product of these two values describes the estimated uncertainty, where values greater than 0.5 are considered acceptable (Fig. 7). Synthetic tests demonstrate

Downloaded from http://gji.oxfordjournals.org/ at Columbia University on June 6, 2016

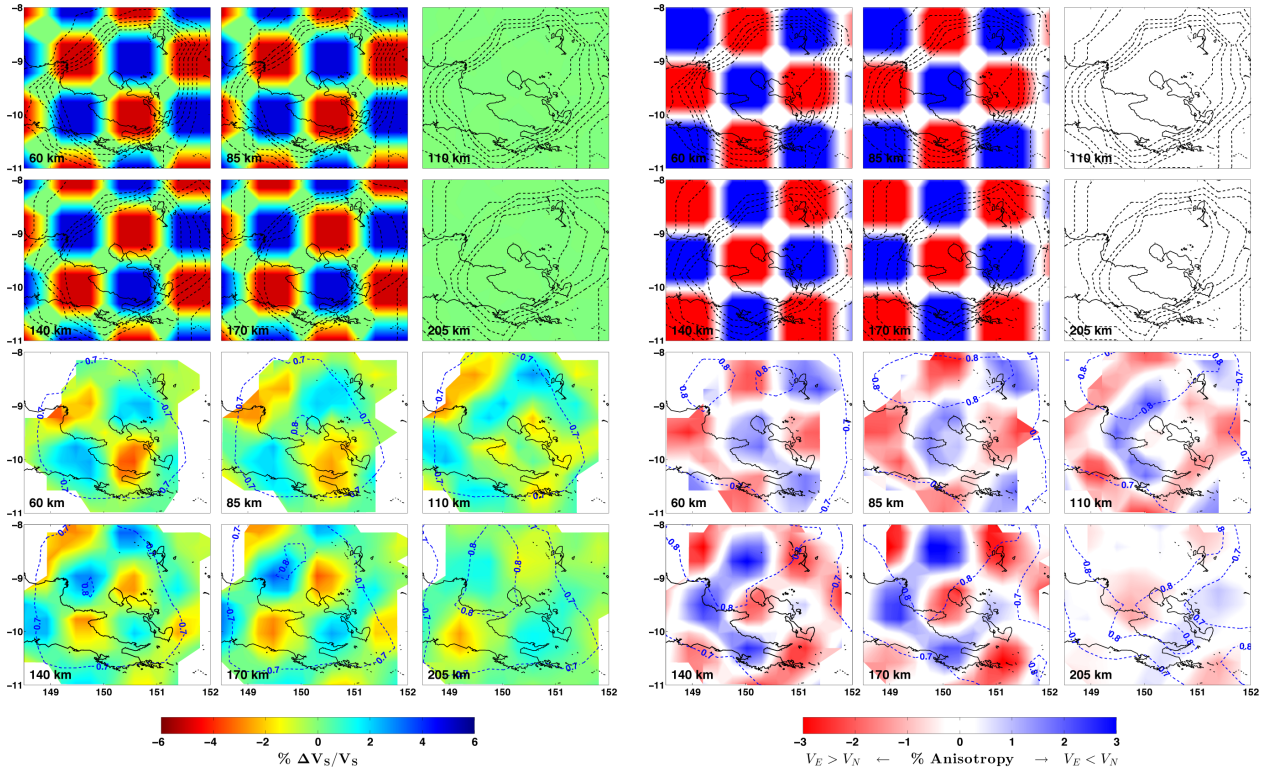

Figure 7. Checkerboard tests for a joint $V_{S_{av}}$ and anisotropy inversion, contoured by semblance. In the well-imaged region with hit quality greater than 0.7, the mean semblance is 0.73, indicating good amplitude and structure recovery. Note the staggering of the V_S and α checkers is preserved in the output model, demonstrating that the two parameters are independently constrained.

that not only are we able to recover input structure but that we can independently resolve velocity and anisotropy heterogeneity with good fidelity (Fig. 7).

We ascertain the depth of heterogeneity *required* by the data by introducing a squeezing depth into the first two iterations of the inversion (Eilon *et al.* 2015). If the data require structure below z_{sq} it will be introduced by later, unconstrained iterations, the final model will have appreciable model norm below z_{sq}, and this deeper structure will significantly contribute to variance reduction. We find that for tests that include squeezing to depths (z_{sq}) of 170 km or greater, >95 per cent of the final variance reduction is achieved with structure above z_{sq}. This indicates that the data require models to contain velocity and anisotropy heterogeneities down to a depth of at least 170 km but that deeper structure does not improve the fit to the data and is not required. In the final inversion, we therefore include a single squeezing step to 170 km depth. By comparing the norm of the structure deeper than z_{sq} before and after squeezing to 170 km we find that 16.4 per cent of the anisotropy heterogeneities, but only 9.05 per cent of the velocity heterogeneities, appear deeper than this depth, suggesting more power in anisotropy variation than velocity variation in the deeper part of the domain. This observation agrees with our expectation that passive rifts do not evince deep velocity signatures, but may accrue strain (and hence anisotropic fabric) at large depths.

5 RESULTS

5.1 Tomographic models

Our preferred models have an overall variance reduction of 87.5 per cent after eight iterations, beyond which point there is negligible improvement in the fit. The reduction in variance for the differential traveltime data and splitting data are approximately equal and the final rms error is 0.41 s. Rms station static differential traveltime is 0.50 s and the distribution of station static values is consistent with receiver function data that show thinned crust beneath the DEI compared to the Papuan Peninsula (Abers *et al.* 2002, 2016). Crustal time excesses at OBS stations on the western Trobriand Platform are due to thick sediments (Fitz & Mann 2013), and <1 s time deficits at stations on the Amphlett Islands and Trobriand Islands (in agreement with the isotropic inversion) indicate fast shallow structure. Rms crustal splitting times is 0.17 s, indicating negligible anisotropy in the crust (although this parameter is damped, even when damping is reduced by 10× the rms crustal splitting is just 0.28 s).

5.1.1 2-D models

We first consider models where along strike variation in velocity and anisotropy is damped to zero (Fig. 8). The resultant models (which achieve a variance reduction of 83.7 per cent) represent a 2-D average of the rift that includes only the most robust structure required by the data. These north–south cross-sections reveal the low-velocity rift axis extending down to ∼170 km depth beneath the DEI and to their south. There is also a well-resolved high-velocity feature in the upper 140 km beneath the north of the array. Within the rift axis delineated by the low velocities, an N–S fast anisotropic fabric extends from depths of ∼250 km to the top of the model, directly beneath the DEI. To the north and south, on the shoulders of the rift, the models reveal shallow E–W fast structure extending off-axis to at least the edges of the well-resolved region. By comparison with the 3-D models, the apparent necking of N–S

Downloaded from http://gji.oxfordjournals.org/ at Columbia University on June 6, 2016

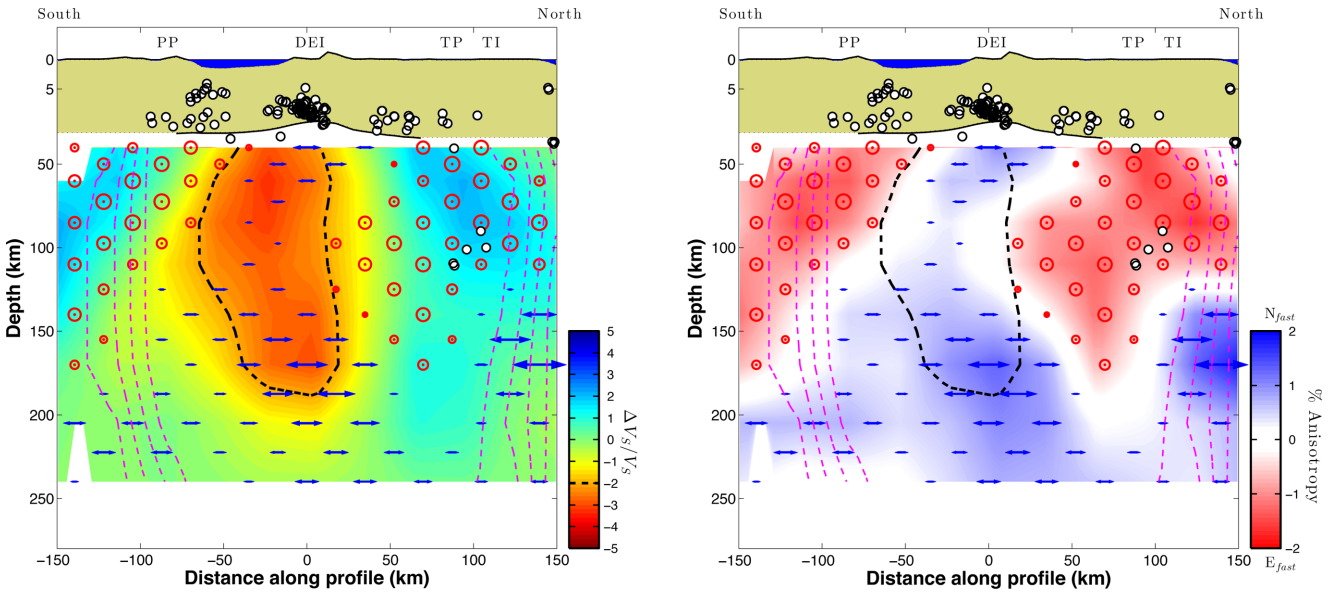

Figure 8. North–south sections through velocity/anisotropy model where heterogeneities are constrained to vary only in 2-D (Section 5.1.1). Black dashed line encloses slow rift axis ($V_{S_{av}} < -2$ per cent), blue arrows and red circles (denoting arrows 'into the page') show N–S-fast or E–W-fast fabric, respectively. 10 per cent hit quality contours shown. White circles: seismicity observed during Woodseis and CDPapua experiments, relocated using hypoDD. The Moho is derived from receiver functions along a N–S transect at 150.5°E. Note scale change at 5 km depth so topography is 3.5× exaggerated. PP: Papuan Peninsula; TP: Trobriand Platform; TI: Trobriand Islands.

fast anisotropy at ∼100 km depth is likely an artefact arising from along strike smoothing combined with slightly heterogeneous ray coverage.

5.1.2 3-D models

The velocity model prominently contains a rift-parallel swath of low velocities beneath Goodenough Basin and the southern DEI that extends westward beneath the Papuan Peninsula (Fig. 9). Within the well-resolved region, the axial material (defined within the $d \ln V_{S_{av}} < -1$ per cent contour) is, on average, ∼3 per cent slower than the layer mean and with increasing depth widens from 120 to 160 km. There is a sharp boundary between the slow rift axis and a large, high-velocity structure in the north of the model; at depths of 60–85 km there is a maximum of 11 per cent velocity contrast between these structures, and a sharp horizontal velocity gradient at the boundary (8 per cent over just 60 km) matching strong backazimuthal variations of differential traveltimes recorded at the latitude of Goodenough Island. The loss of resolution beyond the boundaries of the array means that the northern and western boundaries of the high-velocity feature are poorly constrained but its reduction in amplitude further east than 150.5° suggests that it does not extend as far as the edge of our array. Overall, the imaged structure agrees well with isotropic tomography results but is more coarsely resolved owing to the greater regularisation in this study (Fig. 10).

The anisotropy model reveals a ∼150 km wide region of 1–2 per cent N–S fast anisotropy, with maximum strength ≤4.1 per cent, co-located with the low velocities in the axis of the rift (Fig. 11). This structure spans the width of the model and increases in width and amplitude down to 170 km depth. In the upper 100 km of the model, the N–S fabric extends from eastern Fergusson/Normanby Island northwards to the Trobriand Islands, approximately coinciding with the eastern limit of the high-velocity structure. Elsewhere, on the shoulders of the rift, we image a predominant E–W fabric, although to the south of the rift this is not in a well-resolved region. The strong E–W fabric north of Goodenough Island is co-located with the high-velocity structure.

5.2 Synthetic splitting

As a further check on our tomographic model, we compare measured individual *SKS* splits (Eilon *et al.* 2014) to synthetic *SKS* waveforms propagated through the imaged structure, as follows: rays are traced through the model space using a 1-D velocity profile from (IASP91). Each ray is divided into 10 km segments; for each segment the mean velocity and anisotropy are interpolated from the tomography model and used to calculate the appropriately oriented elastic tensor (eq. A6). We solve the Christoffel equations using the ray propagation vector in each segment, computing the fast and slow velocities and polarisations in the ray-based coordinate system. We then propagate an 8 s Gaussian wavelet along this ray, starting with *P–SV* polarisation and resolving this energy onto the fast and slow polarisations in each segment, with respective propagation velocities. Finally, this arrival is resolved onto north and east channels, and filtering and windowing is applied prior to standard splitting analysis using the Minimum Energy method (Silver & Chan 1991).

We find that the initial polarisation is preserved and there is good agreement between our simplified anisotropy approximation (eq. 5) using a finite-frequency approach and the full solution to the Christoffel equations using a ray-based approach. Splitting time (dT) calculated with finite frequencies is, on average 26 per cent smaller than that calculated with rays, because of intrinsic smoothing. The fast direction (φ) error is very small, as expected for the small incidence angle of *SK(K)S* phases (Fig. 2). This agreement is possible despite the multiple anisotropic layers because of the constraint on the geometry of the anisotropy to be orthogonal (NS-fast or EW-fast), leading to linearly additive splitting. This condition is unlikely to be true in the real Earth (Silver & Savage 1994) and will be a source of error in the analysis.

Downloaded from http://gji.oxfordjournals.org/ at Columbia University on June 6, 2016

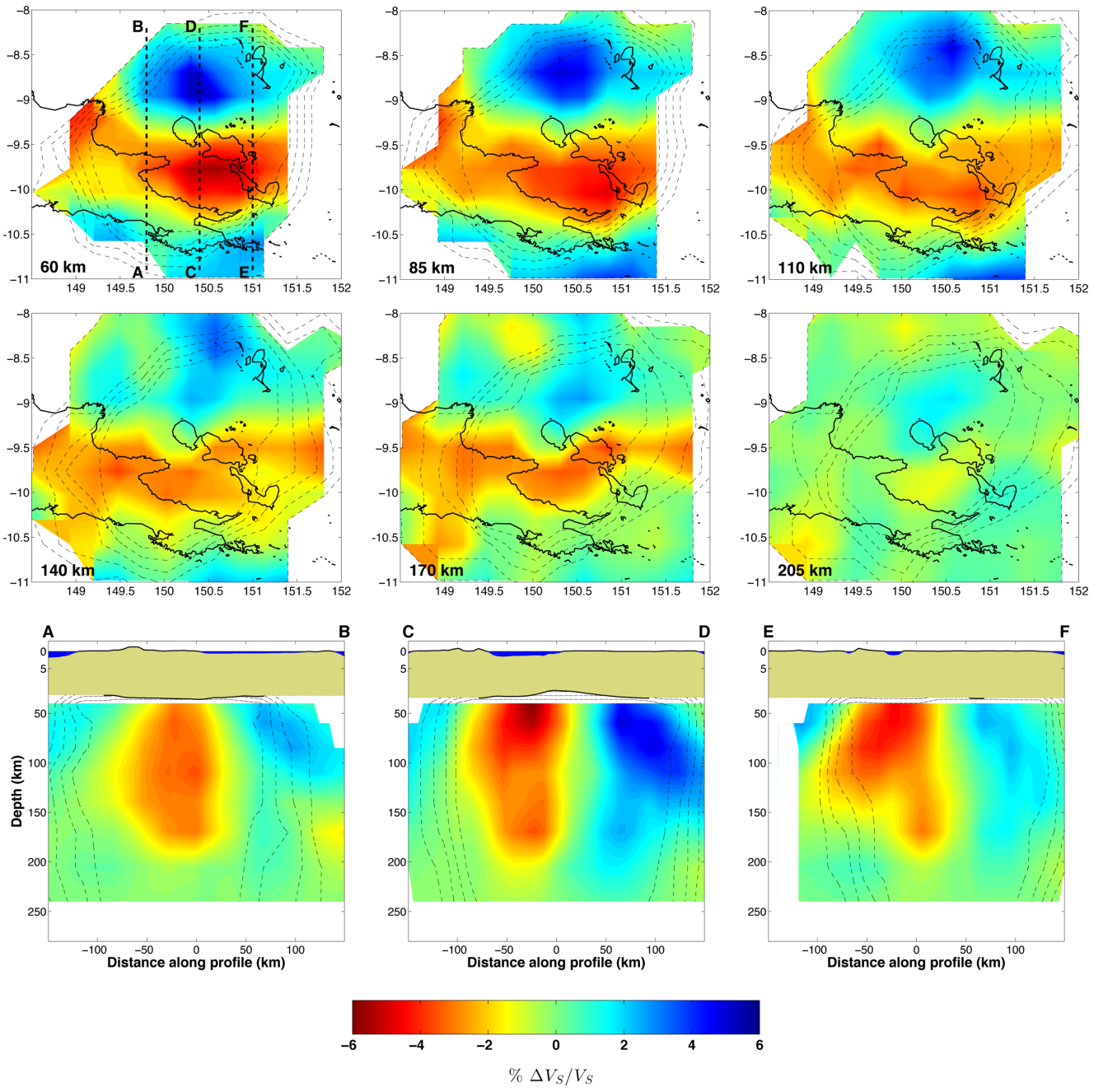

Figure 9. Horizontal and vertical slices showing $\Delta V_{S_{av}}$ from the 3-D anisotropic shear velocity model (Section 5.1.2) with 10 per cent hit quality contours shown.

The mean angular misfit (weighted by measured *dT*) between predicted and observed *SKS* φ is 28.2° ± 25.9 (1σ) demonstrating that the anisotropic velocity model—obtained using only direct *S* arrivals—is in good agreement with the *SKS* measurements (Fig. 3b). The mean predicted *dT* values systematically underestimate the measured values from *SKS* splitting; this discrepancy likely arises from the larger uncertainty in measured *dT* (compared to φ) (Silver & Chan 1991), overdamped model anisotropic structure, and the limited depth extent of the well-resolved model space (Section 4.2). The only location in which there is systematic angular misfit between observed and measured φ is in the northwest of the model where measured splitting ($\varphi \approx 0$) is orthogonal to the E–W fabric in the tomographic model. Much of this misfit comes from arrivals at stations on the Lucansay Islands, close to the edge of our model domain, where the *SKS* rays may be sampling deeper N–S structure associated with overall mantle flow (Eilon *et al.* 2014). Overall, *SKS* data—which were not used in the inversion—offer an independent confirmation of the structure in our models.

6 DISCUSSION

6.1 Rift velocity and anisotropy structure

The models contain a slow shear velocity region demarcating the axis of the rift, consistent with structure in isotropic V_P and V_S

Downloaded from http://gji.oxfordjournals.org/ at Columbia University on June 6, 2016

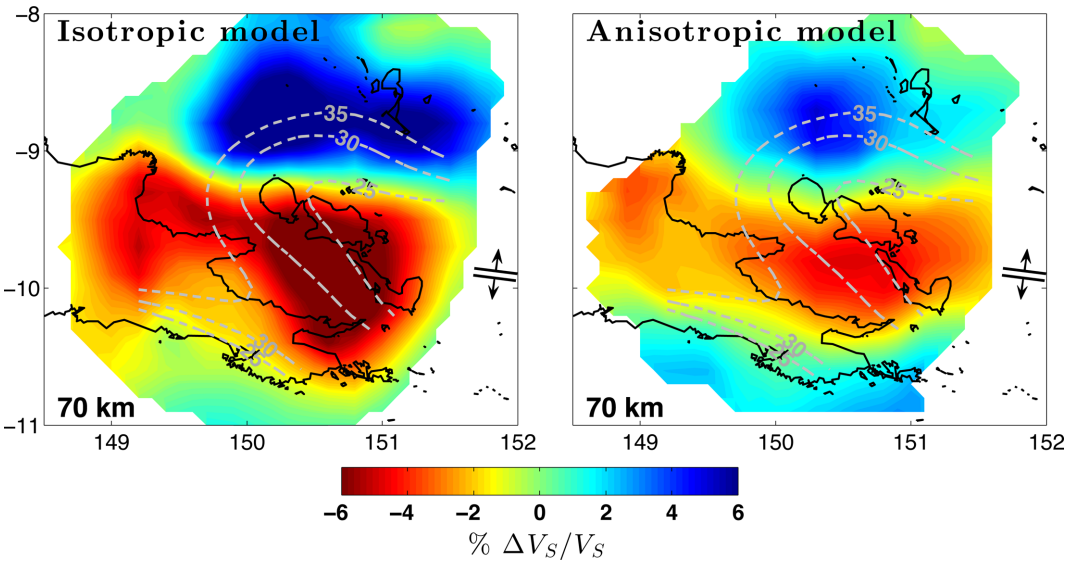

Figure 10. Comparison between imaged V_S variations at 70 km depth from the isotropic inversion (Eilon *et al.* 2015) and 3-D anisotropic inversion (this study). Grey lines: Moho contours (km) for a smooth surface fit to point measurements from a joint receiver function and surface wave inversion (Abers *et al.* 2016).

models (Eilon *et al.* 2015) and aligned with the thinnest Moho (Abers *et al.* 2002, 2016), Holocene volcanic centres and the along-strike extrapolation of the oceanic spreading centres immediately east of the array. A fast feature north of the rift axis is also seen in isotropic models; the large velocity contrast ($\delta V_{S_{\rm av}} = 13$ per cent in these models) with the axial material and the observation of intermediate depth seismicity in this structure are evidence for its being cold lithosphere, possibly a relict slab fragment left over from recent subduction (Eilon *et al.* 2015).

This study shows that the rift axis also contains strong N–S fast fabric with spatial extent very similar to the low-$V_{S_{\rm av}}$ region. The pattern of anisotropy agrees well with shear wave splitting measurements of spreading-parallel fast azimuth on the DEI. We infer that the region of mantle at the centre of the rift has experienced lithospheric removal and asthenospheric upwelling and has also developed a spreading-parallel anisotropic fabric: we are observing the process of lithospheric breakup in the anisotropy signal. As the continent breaks apart, increasing extensional strain and lithospheric thinning result in mantle CPO being simultaneously accrued and advected upwards within the rift axis (Tommasi *et al.* 1999). A positive feedback between temperature, anisotropic viscosity and strain may facilitate this process and explain the congruence of the slow velocity and N–S fast structures.

Models (Blackman & Kendall 2002) and observations (Gaherty *et al.* 2004) have established that spreading-parallel azimuthal anisotropy dominates the shallow upper mantle in the ocean basins. It is an open question how quickly corner flow at ridges (e.g. as envisioned by McKenzie & Sclater 1969) implements a horizontal fabric. Vertical flow of ascending material at the ridge axis should produce radial, rather than azimuthal, anisotropy. However, at the rift axis we observe strong, *shallow* azimuthal anisotropy consistent with spreading-parallel fabric (Fig. 8). This observation, from a region on the cusp of full seafloor spreading, is in agreement with strong azimuthal anisotropy measured on the East Pacific Rise (Wolfe & Solomon 1998) and elsewhere (Nowacki *et al.* 2012). Even accounting for intrinsic smoothing associated with finite-frequency fresnel zones, our results suggest that corner flow efficiently establishes a spreading fabric through extensional shear close to the spreading axis.

This process may be accelerated in continental rifts; Nielsen & Hopper (2004) demonstrate that dehydration and depletion due to melting should increase the viscosity and buoyancy of uppermost mantle within the rift axis. This phenomenon could enhance the shallow establishment of azimuthal anisotropy as it suppresses upwelling and favours predominantly horizontal strain, explaining the observed anisotropic structure.

The N–S fabric may extend below the well-resolved part of the model, which would explain the synthetic *SKS dT* underestimates (Section 5.2) and higher norm in the deeper layers following squeezing (Section 4.2). Our preferred models suggest that anisotropic structure persists deeper than velocity heterogeneities. This observation could result from deteriorating depth resolution of differential traveltime data compared to *SKS* data. Alternatively, it may be evidence for extensional strain being accommodated in the convecting mantle where temperature changes little and deformation yields only small horizontal temperature (and hence, velocity) gradients. Deep fabric may arise from asymmetric mantle flow beneath the moving ridge segment (*cf.* Conder *et al.* 2002). The Woodlark Rift is translating northwards at ∼65 mm yr^{-1} in a hotspot reference frame, resulting in asymmetric flow that could explain deep N–S fabric (Eilon *et al.* 2014).

A limitation of our method is the inability to resolve dip of the anisotropic symmetry axis, which is fixed to be horizontal [implicitly assuming that gradients of strain rate are vertical; Tommasi *et al.* (1999)]. Dip can be detected from the ratio of the first two azimuthal harmonics of the splitting intensity (Chevrot 2000); this measurement is noisy at almost all stations in this study, but there is no evidence suggesting a dip to the symmetry axis (Eilon *et al.* 2014). In principle, the dip could be included in the inversion, but tests demonstrate that our data cannot discern this parameter. Fabric dip would introduce a backazimuthally varying source of error, and (for $<30^\circ$ dip) on average lead to overestimation of isotropic velocity and underestimation of anisotropy strength (Fig. 2). A non-horizontal symmetry axis within this rift may result from corner-flow fabric near the spreading axis (Blackman & Kendall 2002), a vertical component of strain as the lithosphere thins, or melt-rich layers at a dipping lithosphere–asthenosphere boundary (Holtzman & Kendall 2010). Despite these possibilities, shallow or negligible

Downloaded from http://gji.oxfordjournals.org/ at Columbia University on June 6, 2016

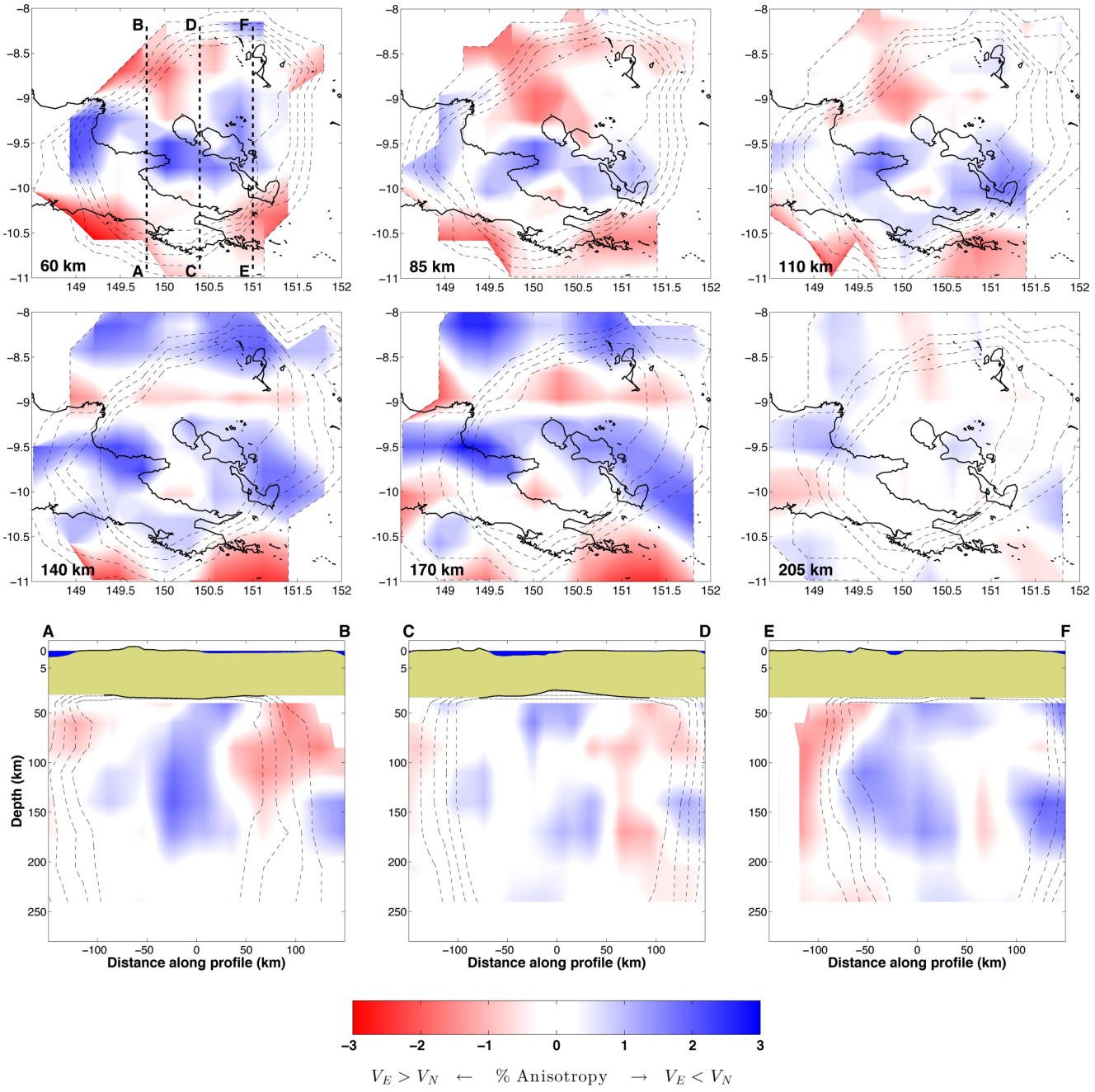

Figure 11. Horizontal and vertical slices through the 3-D anisotropy model (Section 5.1.2) with 10 per cent hit quality contours shown. Positive values (blue) indicate N–S fast and negative values (red) indicate E–W fast.

dip was observed at the East Pacific Rise (Hammond & Toomey 2003).

Unlike other continental rifts such as Rio Grande (Gok *et al.* 2003) or the MER (Kendall *et al.* 2005; Bastow *et al.* 2010; Hammond *et al.* 2010), this rift is not dominated by shallow rift-parallel fabric, often inferred to result from melt lenses aligned normal to spreading (e.g. Kendall *et al.* 2005). Isotropic tomography indicates that this rift is relatively magma-poor (Eilon *et al.* 2015), consistent with low-mantle potential temperature (Ruprecht *et al.* 2013) and volumetrically modest calc-alkaline Holocene volcanism (Smith 1982). The relative paucity of melt and the greater magnitude and rate of extensional strain explain the predominance of spreading-parallel CPO in this rift compared to its tectonic analogues (Eilon *et al.* 2014).

6.2 Rift shoulder structure

The N–S fabric appears to have pushed apart a shallow E–W fabric that now lies north and south beneath the rift shoulders. This geometry indicates that prior to rifting there was an E–W 'frozen-in' lithospheric fabric, likely developed during Eocene–Miocene northward convergence, terrane accretion and lithospheric shortening (Davies & Jaques 1984; Baldwin *et al.* 2012). Observations (Huang *et al.* 2000; Kaviani *et al.* 2009) and simulations (Tommasi *et al.* 1999) indicate development of lithospheric anisotropy with fast azimuth parallel to the strike of orogenic belts—for the Papuan Peninsula this would correspond to an E–W fabric, as observed.

The E–W fast structure northwest of the rift axis is greater in amplitude and depth than the conjugate feature to the south. This

Downloaded from http://gji.oxfordjournals.org/ at Columbia University on June 6, 2016

structure co-locates with the high-$V_{S_{av}}$ relict slab and the boundary between the slab and the rift axis. A north- or south-dipping slab (Eilon *et al.* 2015) would explain the strong E–W fabric: trench-parallel splitting is commonly observed in subduction zones (Long & Silver 2009) and may arise from along-strike flow, *b-type* fabric (Karato *et al.* 2008), tilted radial anisotropy (Song & Kawakatsu 2012), or even intraslab anisotropy (Eakin *et al.* 2016). Although this structure is strong and well resolved in the anisotropy model, it gives rise to the only major discrepancy between synthetic and observed *SKS* measurements (Section 5.2); perhaps because core refracted phases are mostly sampling deeper N–S fabric not traversed by direct *S*. Alternatively, the disagreement could arise from locally intermediate-azimuth (e.g. NE–SW) anisotropic structure in this region being mapped onto our orthogonal basis; this possibility reinforces the importance of using multiple data types to interrogate complex structure. That said, the strength of E–W anisotropy we model in this region indicates that any intermediate-azimuth structure here must have a strongly dominant E–W component, clearly differentiable from anisotropy within the rift axis.

Tectonic constraints imply a S-dipping, E–W striking subduction boundary to the north (Yan & Kroenke 1993), suggesting a fundamentally 2-D geometry is applicable. Despite this, the presence of a relict slab in the northwest may complicate shallow flow fields beneath the rift's northern shoulder. Isotropic V_P tomography and intermediate earthquake locations (Eilon *et al.* 2015) and V_S constraints from this study hint that cold slab temperatures becomes less pronounced east of 150.5°E (Section 5.1.2). This may result from the E–W gradient in extension. Strong, shallow N–S fast anisotropy in the northeast of the model, apparently coincident with the edge of the high-velocity body, could reflect toroidal flow around an eastern edge of the slab or simply extensional strain that extends further north when uninhibited by the presence of a viscous/rigid slab.

The sharp and relatively vertical velocity boundaries demarcating the rift edges imply strain localisation processes involving water, chemical depletion or mechanical controls (Eilon *et al.* 2015). Our results indicate asymmetry between the rift shoulders. The ∼5 per cent $\delta \ln V_S$ between the rift axis and the well-resolved part of the southern shoulder is similar to that observed in other rifts (Bastow *et al.* 2008) and ridges (Nettles & Dziewonski 2008). The velocity gradient between rift axis and shoulder is much greater in the north, due to the large temperature contrast of upwelling asthenosphere juxtaposed against a cold lithospheric fragment.

6.3 Anisotropy–velocity trade-offs

Tomographic studies routinely interpret differential traveltimes as a function of velocity heterogeneity alone. A key component of this study is the quantification of trade-offs between the contributions of velocity and anisotropy to observed traveltimes. Inversions in which anisotropy is damped to zero provide a significantly poorer fit: the variance reduction to δt data achieved by isotropic velocity heterogeneity alone is 69.3 per cent (compared to 86.8 per cent with anisotropy). Inversions in which velocity heterogeneities are damped to zero fit the $dT_{\mathrm{N–E}}$ data only marginally less well (84.6 per cent compared to 87.1 per cent for the full model) as expected from the second-order control of $\Delta V_{S_{av}}$ on splitting. However, these inversions do reduce the differential traveltime variance by 34 per cent despite no velocity heterogeneity, demonstrating that a substantial portion of the signal in the δt data is due to anisotropy alone.

We have previously argued that strong velocity perturbations in this region (as observed in the isotropic inversion—Fig. 10) are explicable by unusually large temperature heterogeneities (Eilon *et al.* 2015). We believe the more muted $\Delta V_{S_{av}}$ in the anisotropic model underestimates true variations. This phenomenon results from the increased regularisation required by the anisotropic inversion, which contains more model parameters. The loss in amplitude is consistent with our synthetic tests (Fig. 7).

The importance of a joint inversion is not only evident from an improved fit to data, but from the differences in observed structure. In models with only isotropic velocity variations, the southern rift shoulder is not clear in V_S, but well defined in the V_P model (Eilon *et al.* 2015). For azimuthally homogeneous data distribution, the effects of azimuthal anisotropy should, to first order, cancel out. However, by computing the average polarisation of waves interacting with each node in the model, we find that the region south of the rift axis is disproportionately illuminated by waves that happen to be polarised N–S, which move slower through the E–W fabric here, counteracting the effect of colder (isotropically faster) structure. In this inversion, once the effects of anisotropy and velocity structure are separated, we retrieve a model with a clearly defined southern boundary to the slow rift axis (Fig. 10) emphasising the localised extension to depth.

7 CONCLUSIONS

We have developed a simple parametrisation of anisotropy and mean shear velocity by describing elastic tensors relevant to upper-mantle fabrics in terms of two orthogonal shear velocities ($V_{\parallel}$ and $V_{\perp}$). This parametrisation yields approximate solutions to the Christoffel equations that are analytically differentiable, allowing efficient calculation of Fréchet derivatives that make up the data kernel of a non-linear inverse problem. By assuming the orientation of the anisotropy, on the basis of prior splitting information and the geometry of the tectonic environment, the anisotropic velocity structure is related to teleseismic *S*-wave differential traveltimes and splitting times measured simultaneously with three-way cross-correlation. These data are iteratively inverted for 3-D velocity and anisotropy heterogeneity, using finite-frequency sensitivity kernels.

This method is applied to the Woodlark Rift, Papua New Guinea, imaging a low-velocity rift axis extending westward from the nearby mid-ocean ridge tip more than 250 km into the continent congruent with shallow Moho, Holocene volcanism and high heat flow. This study reconciles previous isotropic tomography and *SKS* splitting measurements in this rift, providing an important depth control on anisotropy. In agreement with isotropic *P*, *S* and surface wave images, there is a large-velocity contrast between the ∼6 per cent slow rift axis and ∼5 per cent fast cold lithospheric material at >100 km depth to the north. Up to 4 per cent anisotropy with N–S fast azimuth has developed from 50 to 150 km depth within the rift axis, breaking apart a pre-existing lithospheric fabric still evident on the rift shoulders. The congruency of the N–S fabric and the low-velocity structure indicates the co-development of lithospheric thinning and extension-related CPO in the upwelling asthenosphere. The observation of strong, shallow azimuthal anisotropy within the rift axis implies efficient establishment of fabric in a corner-flow

Downloaded from http://gji.oxfordjournals.org/ at Columbia University on June 6, 2016

regime. Jointly inverting for shear velocity and anisotropy allows us to account for, and quantify, trade-offs between the two parameters.

ACKNOWLEDGEMENTS

The authors acknowledge helpful discussions with Ben Holtzman, Roger Buck, Maureen Long, Colton Lynner, Bill Menke and Karen Fischer in the development of the ideas presented in this study. We also thank two anonymous reviewers for thoughtful analysis. This work was supported by NSF grants EAR-0814236 (Abers) and EAR-0708445 (Gaherty). The data used for this project are available through the IRIS DMC under FDSN code ZN (2010-2012).

REFERENCES

Abers, G.A., Ferris, A., Craig, M., Davies, H.L., Lerner-Lam, A.L., Mutter, J.C. & Taylor, B., 2002. Mantle compensation of active metamorphic core complexes at Woodlark rift in Papua New Guinea, *Nature,* **418,** 862–865.

Abers, G.A., Eilon, Z., Gaherty, J.B., Jin, G., Kim, Y.H., Obrebski, M. & Dieck, C., 2016. Southeast Papuan crustal tectonics: imaging extension and buoyancy of an active rift, *J. geophys. Res.,* **121,** 951–971.

Abt, D.L. & Fischer, K.M., 2008. Resolving three-dimensional anisotropic structure with shear wave splitting tomography, *Geophys. J. Int.,* **173**(3), 859–886.

Abt, D.L., Fischer, K.M., Abers, G.A., Strauch, W., Protti, J.M. & González, V., 2009. Shear wave anisotropy beneath Nicaragua and Costa Rica: implications for flow in the mantle wedge, *Geochem. Geophys. Geosyst.,* **10**(5), Q05S15, doi:10.1029/2009GC002375.

Anderson, D.L., 1989. Chapter 15—Anisotropy, in *Theory of the Earth,* pp. 1–34, Blackwell Scientific Publications.

Baldwin, S.L., Webb, L.E. & Monteleone, B.D., 2008. Late Miocene coesite-eclogite exhumed in the Woodlark Rift, *Geology,* **36**(9), 735–738.

Baldwin, S.L., Fitzgerald, P.G. & Webb, L.E., 2012. Tectonics of the New Guinea region, *Annu. Rev. Earth Planet. Sci.,* **40,** 495–520.

Bastow, I.D., Pilidou, S., Kendall, J.M. & Stuart, G.W., 2010. Melt-induced seismic anisotropy and magma assisted rifting in Ethiopia: evidence from surface waves, *Geochem. Geophys. Geosyst.,* **11**(6), doi:10.1029/2010GC003036.

Bastow, I.D., Nyblade, A.A., Stuart, G.W., Rooney, T.O. & Benoit, M.H., 2008. Upper mantle seismic structure beneath the Ethiopian hot spot: rifting at the edge of the African low-velocity anomaly, *Geochem. Geophys. Geosyst.,* **9**(12) Q12022, doi:10.1029/2008GC002107.

Bezada, M.J., Faccenda, M., Toomey, D.R. & Humphreys, E., 2014. Why ignoring anisotropy when imaging subduction zones could be a bad idea, in *AGU Fall Meeting 2014,* 04, abstract #S41D-04.

Blackman, D.K. & Kendall, J.M., 2002. Seismic anisotropy in the upper mantle 2. Predictions for current plate boundary flow models, *Geochem. Geophys. Geosyst.,* **3**(9), doi:10.1029/2001GC000247.

Boyd, O.S., Jones, C.H. & Sheehan, A.F., 2004. Foundering lithosphere imaged beneath the Southern Sierra Nevada, California, USA, *Science,* **305**(5684), 660–662.

Chevrot, S., 2000. Multichannel analysis of shear wave splitting, *J. geophys. Res.,* **105**(21), 21 579–21 590.

Chevrot, S., 2006. Finite-frequency vectorial tomography: a new method for high-resolution imaging of upper mantle anisotropy, *Geophys. J. Int.,* **165**(2), 641–657.

Christensen, N.I., 1984. The magnitude, symmetry and origin of upper mantle anisotropy based on fabric analyses of ultramafic tectonites, *Geophys. J. R. astr. Soc.,* **76**(1), 89–111.

Conder, J.A., Forsyth, D.W. & Parmentier, E.M., 2002. Asthenospheric flow and asymmetry of the East Pacific Rise, MELT area, *J. geophys. Res.,* **107**(B12), doi:10.1029/2001JB000807.

Davies, H.L. & Jaques, A.L., 1984. Emplacement of ophiolite in Papua New Guinea, *Geol. Soc. Lond. Spec. Publ.,* **13**(1), 341–349.

Eakin, C.M., Long, M.D., Scire, A., Beck, S.L., Wagner, L.S., Zandt, G. & Tavera, H., 2016. Internal deformation of the subducted Nazca slab inferred from seismic anisotropy, *Nat. Geosci.,* **9,** 56–59.

Eilon, Z., Abers, G.A., Jin, G. & Gaherty, J.B., 2014. Anisotropy beneath a highly extended continental rift, *Geochem. Geophys. Geosyst.,* **15,** 545–564.

Eilon, Z., Abers, G.A., Gaherty, J.B. & Jin, G., 2015. Imaging continental breakup using teleseismic body waves: the Woodlark Rift, Papua New Guinea, *Geochem. Geophys. Geosyst.,* **16,** doi:10.1002/2015GC005835.

Favier, N. & Chevrot, S., 2003. Sensitivity kernels for shear wave splitting in transverse isotropic media, *Geophys. J. Int.,* **153,** 213–228.

Ferris, A., Abers, G.A., Zelt, B., Taylor, B. & Roecker, S.W., 2006. Crustal structure across the transition from rifting to spreading: the Woodlark rift system of Papua New Guinea, *Geophys. J. Int.,* **166**(2), 622–634.

Fitz, G. & Mann, P., 2013. Tectonic uplift mechanism of the Goodenough and Fergusson Island gneiss domes, eastern Papua New Guinea: constraints from seismic reflection and well data, *Geochem. Geophys. Geosyst.,* **14**(10), 3969–3995.

Foley, B.J. & Long, M.D., 2011. Upper and mid-mantle anisotropy beneath the Tonga slab, *Geophys. Res. Lett.,* **38**(2), L02303, doi:10.1029/2010GL046021.

Fouch, M.J. & Fischer, K.M., 1996. Mantle anisotropy beneath northwest Pacific subduction zones, *J. geophys. Res.,* **101**(B7), 15 987–16 002.

Gaherty, J.B., Lizarralde, D., Collins, J.A., Hirth, G. & Kim, S., 2004. Mantle deformation during slow seafloor spreading constrained by observations of seismic anisotropy in the western Atlantic, *Earth planet. Sci. Lett.,* **228**(3), 255–265.

Gao, S.S., Liu, H., Rigor, A.W., Mordvinova, V.V., Kozhevnikov, V.M. & Logatchev, N.A., 1997. SKS splitting beneath continental rift zones, *J. geophys. Res.,* **102,** 22 781–22 797.

Gok, R., Ni, J.F., West, M. & Sandvol, E., 2003. Shear wave splitting and mantle flow beneath the LA RISTRA, *Geophys. Res. Lett.,* **30**(12), 1614, doi:10.1029/2002GL016616.

Gordon, S.M., Little, T.A., Hacker, B.R. & Bowring, S.A., 2012. Multi-stage exhumation of young UHP–HP rocks: timescales of melt crystallization in the D'Entrecasteaux Islands, southeastern Papua New Guinea, *Earth planet. Sci. Lett.,* **351–352,** 237–246.

Hammond, W.C. & Toomey, D.R., 2003. Seismic velocity anisotropy and heterogeneity beneath the Mantle Electromagnetic and Tomography Experiment (MELT) region of the East Pacific Rise from analysis of P and S body waves, *J. geophys. Res.,* **108**(B4), 2176, doi:10.1029/2002JB001789.

Hammond, J.O.S., Kendall, J.M., Angus, D. & Wookey, J., 2010. Interpreting spatial variations in anisotropy: insights into the Main Ethiopian Rift from SKS waveform modelling, *Geophys. J. Int.,* **181**(3), 1701–1712.

Hammond, J.O.S., Kendall, J.M. & Wookey, J., 2014. Differentiating flow, melt, or fossil seismic anisotropy beneath Ethiopia, *Geochem. Geophys. Geosyst.,* **15,** 1878–1894.

Hansen, L.N., Zhao, Y.-H., Zimmerman, M.E. & Kohlstedt, D.L., 2014. Protracted fabric evolution in olivine: implications for the relationship among strain, crystallographic fabric, and seismic anisotropy, *Earth planet. Sci. Lett.,* **387,** 157–168.

Holtzman, B.K. & Kendall, J.M., 2010. Organized melt, seismic anisotropy, and plate boundary lubrication, *Geochem. Geophys. Geosyst.,* **11,** Q0AB06, doi:10.1029/2010GC003296.

Huang, W.C. *et al.*, 2000. Seismic polarization anisotropy beneath the central Tibetan Plateau, *J. geophys. Res.,* **105**(B12), 27 979–27 989.

Ismaïl, W.B. & Mainprice, D., 1998. An olivine fabric database: an overview of upper mantle fabrics and seismic anisotropy, *Tectonophysics,* **296**(1–2), 145–157.

Karato, S., Jung, H. & Katayama, I., 2008. Geodynamic significance of seismic anisotropy of the upper mantle: new insights from laboratory studies, *Annu. Rev. Earth Planet. Sci.,* **36,** 59–95.

Kaviani, A., Hatzfeld, D., Paul, A., Tatar, M. & Priestley, K., 2009. Shear-wave splitting, lithospheric anisotropy, and mantle deformation beneath the Arabia-Eurasia collision zone in Iran, *Earth planet. Sci. Lett.,* **286**(3–4), 371–378.

Downloaded from http://gji.oxfordjournals.org/ at Columbia University on June 6, 2016

Kendall, J.M., Stuart, G.W., Ebinger, C.J., Bastow, I.D. & Keir, D., 2005. Magma-assisted rifting in Ethiopia, *Nature,* **433**(7022), 146–148.

Kendall, J.M., Pilidou, S., Keir, D., Bastow, I.D., Stuart, G.W. & Ayele, A., 2006. Mantle upwellings, melt migration and the rifting of Africa: insights from seismic anisotropy, *Geol. Soc. Lond. Spec. Publ.,* **259**(1), 55–72.

Kustowski, B., Ekström, G. & Dziewonski, A.M., 2008. Anisotropic shear-wave velocity structure of the Earth's mantle: a global model, *J. geophys. Res.,* **113**(B6), B06306, doi:10.1029/2007JB005169.

Long, M.D., 2010. Frequency-dependent shear wave splitting and heterogeneous anisotropic structure beneath the Gulf of California region, *Phys. Earth planet. Inter.,* **182,** 59–72.

Long, M.D. & Silver, P.G., 2009. Mantle flow in subduction systems: the subslab flow field and implications for mantle dynamics, *J. geophys. Res.,* **114**(B10), B10312, doi:10.1029/2008JB006200.

Long, M.D., De Hoop, M.V. & van der Hilst, R.D., 2008. Wave-equation shear wave splitting tomography, *Geophys. J. Int.,* **172**(1), 311–330.

Love, A., 1927. *A Treatise on the Mechanical Theory of Elasticity,* Cambridge Univ. Press.

Lynner, C. & Long, M.D., 2014. Sub-slab anisotropy beneath the Sumatra and circum-Pacific subduction zones from source-side shear wave splitting observations, *Geochem. Geophys. Geosyst.,* **15,** 2262–2281.

Lynner, C. & Long, M.D., 2015. Heterogeneous seismic anisotropy in the transition zone and uppermost lower mantle: evidence from South America, Izu-Bonin and Japan, *Geophys. J. Int.,* **201**(3), 1545–1552.

Maupin, V. & Park, J., 2007. Theory and observations—wave propagation in anisotropic media, in *Treatise on Geophysics,* Vol. 1, pp. 289–321, Elsevier.

Mavko, G., Mukerji, T. & Dvorkin, J., 2009. *The Rock Physics Handbook,* Tools for Seismic Analysis of Porous Media, 2nd edn, Cambridge Univ. Press.

McKenzie, D.P. & Sclater, J.G., 1969. Heat flow in the eastern pacific and sea floor spreading, *Bull. Volcanol.,* **33**(1), 101–117.

Menke, W., 1984. *Geophysical Data Analysis: Discrete Inverse Theory,* 1st edn, Academic Press.

Menke, W., 2012. *Geophysical Data Analysis: Discrete Inverse Theory,* MATLAB Edition, 3rd edn, Academic Press.

Menke, W. & Eilon, Z., 2015. Relationship between data smoothing and the regularization of inverse problems, *Pure appl. Geophys.,* doi:10.1007/s00024-015-1059-0.

Mensch, T. & Rasolofosaon, P., 1997. Elastic-wave velocities in anisotropic media of arbitrary symmetry—generalization of Thomsen's parameters ε, δ and γ, *Geophys. J. Int.,* **128,** 43–64.

Montagner, J.P., Marty, B. & Stutzmann, E., 2007. Mantle upwellings and convective instabilities revealed by seismic tomography and helium isotope geochemistry beneath eastern Africa, *Geophys. Res. Lett.,* **34,** L21303, doi:10.1029/2007GL031098.

Nettles, M. & Dziewonski, A.M., 2008. Radially anisotropic shear velocity structure of the upper mantle globally and beneath North America, *Geophys. Res. Lett.,* **113,** B02303, doi:10.1029/2006JB004819.

Nielsen, T.K. & Hopper, J.R., 2004. From rift to drift: mantle melting during continental breakup, *Geochem. Geophys. Geosyst.,* **5**(7), Q07003, doi:10.1029/2003GC000662.

Nowacki, A., Kendall, J.M. & Wookey, J., 2012. Mantle anisotropy beneath the Earth's mid-ocean ridges, *Earth planet. Sci. Lett.,* **317,** 56–67.

Nowacki, A., Kendall, J.M., Wookey, J. & Pemberton, A., 2015. Mid-mantle anisotropy in subduction zones and deep water transport, *Geochem. Geophys. Geosyst.,* **16,** doi:10.1002/2014GC005667.

Panning, M. & Romanowicz, B., 2006. A three-dimensional radially anisotropic model of shear velocity in the whole mantle, *Geophys. J. Int.,* **167**(1), 361–379.

Petersen, K.D. & Buck, W.R., 2015. Eduction, extension and exhumation of ultra-high pressure rocks in metamorphic core complexes due to subduction initiation, *Geochem. Geophys. Geosyst.,* **16,** 2564–2581.

Pozgay, S.H., Wiens, D.A. & Conder, J.A., 2007. Complex mantle flow in the Mariana subduction system: evidence from shear wave splitting, *Geophys. J. Int.,* **170,** 371–386.

Pratt, R.G. & Chapman, C.H., 1992. Traveltime tomography in anisotropic media—II. Application, *Geophys. J. Int.,* **109**(1), 20–37.

Ruprecht, P., Plank, T.A., Jin, G. & Abers, G.A., 2013. Rifting and UHP exhumation in Eastern Papua New Guinea: temperature and pressure constraints from primitive magmas, in *AGU Fall Meeting 2013,* abstract #T21B–2559.

Schmandt, B. & Humphreys, E., 2010. Seismic heterogeneity and small-scale convection in the southern California upper mantle, *Geochem. Geophys. Geosyst.,* **11**(5), Q05004, doi:10.1029/2010GC003042.

Silver, P.G. & Chan, W.W., 1991. Shear wave splitting and subcontinental mantle deformation, *Geophys. Res. Lett.,* **96**(B10), 16 429–16 454.

Silver, P.G. & Long, M.D., 2011. The non-commutivity of shear wave splitting operators at low frequencies and implications for anisotropy tomography, *Geophys. J. Int.,* **184**(3), 1415–1427.

Silver, P.G. & Savage, M.K., 1994. The interpretation of shear-wave splitting parameters in the presence of two anisotropic layers, *Geophys. J. Int.,* **119**(3), 949–963.

Smith, I.E., 1982. Volcanic evolution in eastern Papua, *Tectonophysics,* **87**(1), 315–333.

Song, T. R.A. & Kawakatsu, H., 2012. Subduction of oceanic asthenosphere: evidence from sub-slab seismic anisotropy, *Geophys. Res. Lett.,* **39**(17), doi:10.1029/2012GL052639.

Taylor, B., Goodliffe, A.M. & Martinez, F., 1999. How continents break up: insights from Papua New Guinea, *J. geophys. Res.,* **104**(B4), 7497–7512.

Thomsen, L., 1986. Weak elastic anisotropy, *Geophysics,* **51**(10), 1954–1966.

Tommasi, A., Tikoff, B. & Vauchez, A., 1999. Upper mantle tectonics: three-dimensional deformation, olivine crystallographic fabrics and seismic properties, *Earth planet. Sci. Lett.,* **168**(1), 173–186.

Tommasi, A., Mainprice, D., Canova, G. & Chastel, Y., 2000. Viscoplastic self-consistent and equilibrium-based modeling of olivine lattice preferred orientations—implications for the upper mantle seismic anisotropy, *J. geophys. Res.,* **105**(B4), 7893–7908.

VanDecar, J.C. & Crosson, R.S., 1990. Determination of teleseismic relative phase arrival times using multi-channel cross-correlation and least squares, *Bull. seism. Soc. Am.,* **80**(1), 150–169.

Vauchez, A., Tommasi, A., Barruol, G. & Maumus, J., 2000. Upper mantle deformation and seismic anisotropy in continental rifts, *Phys. Chem. Earth A: Solid Earth Geod.,* **25**(2), 111–117.

Vidale, J.E., 1986. Complex polarization analysis of particle motion, *Bull. seism. Soc. Am.,* **76**(5), 1393–1405.

Wang, J. & Zhao, D., 2013. P-wave tomography for 3-D radial and azimuthal anisotropy of Tohoku and Kyushu subduction zones, *Geophys. J. Int.,* **193**(3), 1166–1181.

Wolfe, C.J. & Solomon, S.C., 1998. Shear-wave splitting and implications for mantle flow beneath the MELT region of the East Pacific Rise, *Science,* **280**(5367), 1230–1232.

Yan, C.Y. & Kroenke, L.W., 1993. A plate tectonic reconstruction of the Southwest Pacific, 0–100 Ma, *Proc. Ocean Drill. Program, Sci. Results,* **130,** 697–709.

Yang, Y., Zhu, L., Su, Y., Chen, H. & Wang, Q., 2015. Crustal anisotropy estimated by splitting of Ps-converted waves on seismogram and an application to SE Tibetan plateau, *J. Asian Earth Sci.,* doi:10.1016/j.jseaes.2015.03.016.

Zelt, C.A., 1998. Lateral velocity resolution from three-dimensional seismic refraction data, *Geophys. J. Int.,* **135**(3), 1101–1112.

Zhao, D., Yu, S. & Liu, X., 2015. Seismic anisotropy tomography: new insight into subduction dynamics, *Gondwana Res.,* doi:10.1016/j.gr.2015.05.008.

Downloaded from http://gji.oxfordjournals.org/ at Columbia University on June 6, 2016

APPENDIX A: APPROXIMATION OF ANISOTROPIC VELOCITIES

Here, we derive an approximation to the velocities of a split shear wave, as a function of propagation direction (ζ) and just two parameters ($V_{S_{\rm av}}$ and α) describing the mean shear velocity and the magnitude of the anisotropy in terms of the orthogonal velocities $V_\perp$ and $V_\parallel$. First, we create an elastic tensor with hexagonal symmetry from just these two parameters, making some assumptions. Second, we compute the solutions, $V_S(\zeta, V_\perp, V_\parallel)$ to the Christoffel equations for this elastic tensor. Finally, we find approximate solutions as functions of $V_\perp$ and $V_\parallel$ that closely match the true solutions. These approximate solutions are chosen for their simple functional form, permitting analytic expressions of the gradients of velocities (and, hence, traveltimes) to be found. For the purposes of notational simplicity, we will define $x \equiv V_\perp$ and $y \equiv V_\parallel$.

Consider an anisotropic medium defined by a stiffness matrix using the Love parameters, A, C, F, L and N (Love 1927). These five independent parameters are sufficient to define the elastic tensor in Voigt notation:

$$\begin{pmatrix} A & (A-2N) & F & 0 & 0 & 0 \\ (A-2N) & A & F & 0 & 0 & 0 \\ F & F & C & 0 & 0 & 0 \\ 0 & 0 & 0 & L & 0 & 0 \\ 0 & 0 & 0 & 0 & L & 0 \\ 0 & 0 & 0 & 0 & 0 & N \end{pmatrix}. \tag{A1}$$

The Love parameters are simply related to the velocities of P and S waves travelling along, or perpendicular to, symmetry axes:

$$\begin{aligned} V_{S\parallel} &= \sqrt{L/\rho} \\ V_{S\perp} &= \sqrt{N/\rho} \\ V_{P\parallel} &= \sqrt{C/\rho} \\ V_{P\perp} &= \sqrt{A/\rho} \end{aligned} \tag{A2}$$

and $F = \eta(A - 2L)$. Assuming $\eta = 1$, $V_{P_{\rm av}} = \nu V_{S_{\rm av}}$ and equal P and S anisotropy [consistent with natural and synthetic samples; Anderson (1989); Ismaïl & Mainprice (1998); Tommasi *et al.* (2000)], we define $x \equiv V_{S_{\rm av}}(1-\alpha)$ and $y \equiv V_{S_{\rm av}}(1+\alpha)$, giving

$$\begin{aligned} A &= \rho\nu^2 x^2 \\ C &= \rho\nu^2 y^2 \\ L &= \rho y^2 \\ N &= \rho x^2 \\ F &= \rho(\nu^2 x^2 - 2y^2). \end{aligned} \tag{A3}$$

These give precisely the same results as the treatment of Panning & Romanowicz (2006), where their anisotropic parameters are related to ours by:

$$\begin{aligned} \xi &= \frac{V_{S\perp}^2}{V_{S\parallel}^2} = \left(\frac{1-\alpha}{1+\alpha}\right)^2 \\ \phi &= \frac{V_{P\parallel}^2}{V_{P\perp}^2} = \left(\frac{1+\alpha}{1-\alpha}\right)^2 = \frac{1}{\xi} \\ V_{S_{\rm voigt-av}}^2 &= \frac{2V_{S\parallel}^2 + V_{S\perp}^2}{3} = V_{S_{\rm av}}^2\left(1 + \frac{2}{3}\alpha + \alpha^2\right) \\ V_{P_{\rm voigt-av}}^2 &= \frac{V_{P\parallel}^2 + 4V_{P\perp}^2}{5} = \nu^2\, V_{S_{\rm av}}^2\left(1 - \frac{6}{5}\alpha + \alpha^2\right) \end{aligned} \tag{A4}$$

and whereas their tensor is symmetric about the (3) direction, ours is symmetric about the (1) direction. (N.B. their 'ϕ' is not the same as the direction of the fast azimuth, as ϕ is defined elsewhere in this paper. Their η is identical to ours.)

The above expressions define velocities of waves propagating along symmetry axes. We substitute the Love parameters into expressions for V_{SV} and V_{SH} as a function of angle, ζ, between the propagation direction and the hexagonal symmetry axis (Mavko *et al.* 2009):

$$\begin{aligned} V_{SH}(\zeta) &= \sqrt{\left(N\sin^2\zeta + L\cos^2\zeta\right)/\rho} \\ V_{SV}(\zeta) &= \sqrt{\left(A\sin^2\zeta + C\sin^2\zeta + L - \sqrt{\left((A-L)\sin^2\zeta - (C-L)\cos^2\zeta\right)^2 + (F+L)^2\sin^2 2\zeta}\right)/2\rho} \end{aligned} \tag{A5}$$

to get precise formulae for the solutions to the Christoffel equations. The equation for V_{SH} is straightforward and may be computed precisely. However, it is desirable to simplify the expression for V_{SV}; we approximate V_{SV} as a function sinusoidally varying with 90° periodicity between

Downloaded from http://gji.oxfordjournals.org/ at Columbia University on June 6, 2016

y at 0° and 90° and $V_{SV}|_{\zeta=45^\circ}$ at 45°:

$$V_{SH} = \sqrt{(x\sin\zeta)^2 + (y\cos\zeta)^2}$$
$$V_{SV} \approx \sqrt{(y\cos 2\zeta)^2 + \left(V_{SV}|_{\zeta=45^\circ}\sin 2\zeta\right)^2}. \tag{A6}$$

We calculate the value of $V_{SV}|_{\zeta=45^\circ}$ as a function of x and y and ν:

$$\begin{aligned} Vs_V|_{\zeta=45^\circ} &= \sqrt{\left(A + C + 2L - \sqrt{(A-C)^2 + 4(A-L)^2}\right)/4\rho} \\ &= \frac{1}{2}\sqrt{\nu^2x^2 + \nu^2y^2 + 2y^2 - \sqrt{\nu^4\left(x^2-y^2\right)^2 + 4\left(\nu^2x^2 - y^2\right)^2}} \\ &\approx \frac{1}{2}\sqrt{\nu^2x^2 + \nu^2y^2 + 2y^2 - \sqrt{4\left(\nu^2x^2 - y^2\right)^2}} \\ &= \frac{1}{2}\sqrt{\nu^2\left(y^2 - x^2\right) + 4y^2} \end{aligned} \tag{A7}$$

where the approximation made in the third step is valid for values of anisotropy less than 10 per cent. Substituting back into eq. (A6), we have:

$$V_{SH} = \sqrt{x^2\sin^2\zeta + y^2\cos^2\zeta}$$
$$V_{SV} \approx \sqrt{y^2\cos^2 2\zeta + \left(\nu^2\left[y^2 - x^2\right]/4 + y^2\right)\sin^2 2\zeta} \tag{A8}$$

where this approximation introduces an error of <0.3 per cent for $\zeta > 47^\circ$ or $\zeta < 15^\circ$ (Fig. 2). For a horizontal symmetry axis, $\zeta = 90 -$ *incidence angle*, and so the approximation introduces negligible error for teleseismic rays in the uppermost mantle. Note that at the extremum of incidence perpendicular to the symmetry axis ($\zeta = 90^\circ$), the expressions simplify to $V_{SH} = x$ and $V_{SV} = y$, and at the extremum of incidence parallel to the symmetry axis ($\zeta = 0^\circ$), $V_{SH} = V_{SV} = y$.

APPENDIX B: TRAVELTIMES AND DERIVATIVES

For a ray travelling through the anisotropic medium we have described, eq. (5) leads to the following expressions for differential traveltimes for shear waves polarised perpendicular (E–W) or parallel (N–S) to the symmetry axis:

$$\delta T_{\mathrm{E}} = \int \frac{\mathrm{d}s}{\left(u^2y^2 + (1-u^2)x^2\right)^{1/2}} - \int \frac{\mathrm{d}s}{V_{S_{\mathrm{ref}}}}$$
$$\delta T_{\mathrm{N}} \approx \int \frac{\mathrm{d}s}{\left(y^2 + \nu^2u^2(1-u^2)\left(y^2-x^2\right)\right)^{1/2}} - \int \frac{\mathrm{d}s}{V_{S_{\mathrm{ref}}}} \tag{B1}$$

and $dT_{\mathrm{N-E}} = \delta T_{\mathrm{N}} - \delta T_{\mathrm{E}}$. Velocities x and y vary along the ray path s, as does the parameter describing propagation direction, u. By inspection it is evident that for vertically incident waves ($i = 0$ and so $u = 0$) the traveltimes reduce to $T_{\mathrm{E}} = \int \mathrm{d}s/x$ and $T_{\mathrm{N}} = \int \mathrm{d}s/y$, as required. The Fréchet kernels in terms of x and y are:

$$\begin{aligned} \frac{\partial\,\delta T_{\mathrm{E}}}{\partial x} &= -\int \frac{\left(1-u^2\right)x}{\left(u^2y^2 + (1-u^2)x^2\right)^{3/2}}\,\mathrm{d}s \\ \frac{\partial\,\delta T_{\mathrm{E}}}{\partial y} &= -\int \frac{u^2y}{\left(u^2y^2 + (1-u^2)x^2\right)^{3/2}}\,\mathrm{d}s \\ \frac{\partial\,\delta T_{\mathrm{N}}}{\partial x} &= \int \frac{\nu^2u^2(1-u^2)x}{\left(y^2 + \nu^2u^2(1-u^2)\left(y^2-x^2\right)\right)^{3/2}}\,\mathrm{d}s \\ \frac{\partial\,\delta T_{\mathrm{N}}}{\partial y} &= -\int \frac{\left(1 + \nu^2u^2(1-u^2)\right)y}{\left(y^2 + \nu^2u^2(1-u^2)\left(y^2-x^2\right)\right)^{3/2}}\,\mathrm{d}s \\ \frac{\partial\,dT_{\mathrm{N-E}}}{\partial x} &= \frac{\partial\,\delta T_{\mathrm{N}}}{\partial x} - \frac{\partial\,\delta T_{\mathrm{E}}}{\partial x} \\ \text{and}\quad \frac{\partial\,dT_{\mathrm{N-E}}}{\partial y} &= \frac{\partial\,\delta T_{\mathrm{N}}}{\partial y} - \frac{\partial\,\delta T_{\mathrm{E}}}{\partial y} \end{aligned} \tag{B2}$$

APPENDIX C: THREE-WAY CROSS-CORRELATION

A shear wave with intermediate polarisation (e.g. $\psi = 45^\circ$) travelling through an anisotropic medium with principal directions (also known as 'null directions') N–S and E–W will be split into two quasi-shear pulses that arrive at station i at distinct arrival times T_{N}^i and T_{E}^i. The splitting time, $dT_{\mathrm{N-E}}^i$, can be measured by cross-correlating the arrivals on N–S and E–W components, which should have identical waveforms

Downloaded from http://gji.oxfordjournals.org/ at Columbia University on June 6, 2016

(although they may have different amplitudes, depending on ψ). Arrivals on a given component may also vary in time between different stations, reflecting local velocity heterogeneities. For a given component (e.g. N–S), the differential traveltime between stations i and j is $T_{\mathrm{N}}^{i} - T_{\mathrm{N}}^{j} = \delta T_{\mathrm{N}}^{i-j}$; this value can be measured by cross-correlating arrivals on the N–S channel at different stations.

Therefore, for M stations there are $2M$ unknowns (or *model parameters*): the times of N–S and E–W arrivals at each station. There are M^2 data measurements that can be made in total: $M(M-1)/2$ from cross-correlating N–S arrivals between all station–station pairs, the same number again for all E–W arrivals and an additional M splitting times. These M^2 measurements can be used to simultaneously and self-consistently solve for differential arrival times and splitting times. This is a mixed-determined problem (Menke 1984): differential arrival times are overdetermined, but average arrival time is underdetermined. Therefore, an appropriate inversion strategy is to use a least-squares approach with the constraint that the average of, say, the N–S differential traveltimes is zero, similar to VanDecar & Crosson (1990).

We construct the equation $\mathbf{Gm} = \mathbf{d}$:

$$
\begin{array}{l}
 \\
\delta T_{\mathrm{N}}^{i-j} \\
 \\
 \\
\delta T_{\mathrm{E}}^{i-j} \\
 \\
 \\
d T_{\mathrm{N-E}}^{i} \\
 \\
 \\
\text{constraint} \\
\end{array}
\overbrace{\begin{array}{ccccc}
1 & -1 & 0 & \cdots & 0 \\
0 & 1 & -1 & \cdots & 0 \\
1 & 0 & -1 & \cdots & 0 \\
\vdots & \vdots & \vdots & \ddots & \vdots \\
0 & 0 & 0 & \cdots & 0 \\
0 & 0 & 0 & \cdots & 0 \\
0 & 0 & 0 & \cdots & 0 \\
\vdots & \vdots & \vdots & \ddots & \vdots \\
1 & 0 & 0 & \cdots & 0 \\
0 & 1 & 0 & \cdots & 0 \\
0 & 0 & 1 & \cdots & 0 \\
\vdots & \vdots & \vdots & \ddots & \vdots \\
0 & 0 & 0 & \cdots & 1 \\
1 & 1 & 1 & \cdots & 1
\end{array}}^{T_{\mathrm{N}}^{i}}
\overbrace{\begin{array}{ccccc}
0 & 0 & 0 & \cdots & 0 \\
0 & 0 & 0 & \cdots & 0 \\
0 & 0 & 0 & \cdots & 0 \\
\vdots & \vdots & \vdots & \ddots & \vdots \\
1 & -1 & 0 & \cdots & 0 \\
0 & 1 & -1 & \cdots & 0 \\
1 & 0 & -1 & \cdots & 0 \\
\vdots & \vdots & \vdots & \ddots & \vdots \\
-1 & 0 & 0 & \cdots & 0 \\
0 & -1 & 0 & \cdots & 0 \\
0 & 0 & -1 & \cdots & 0 \\
\vdots & \vdots & \vdots & \ddots & \vdots \\
0 & 0 & 0 & \cdots & -1 \\
0 & 0 & 0 & \cdots & 0
\end{array}}^{T_{\mathrm{E}}^{i}}
\begin{pmatrix}
T_{\mathrm{N}}^{1} \\ T_{\mathrm{N}}^{2} \\ T_{\mathrm{N}}^{3} \\ \vdots \\ T_{\mathrm{N}}^{M} \\ T_{\mathrm{E}}^{1} \\ T_{\mathrm{E}}^{2} \\ T_{\mathrm{E}}^{3} \\ \vdots \\ T_{\mathrm{E}}^{M}
\end{pmatrix}
=
\begin{pmatrix}
\delta T_{\mathrm{N}}^{1-2} \\ \delta T_{\mathrm{N}}^{2-3} \\ \delta T_{\mathrm{N}}^{1-3} \\ \vdots \\ \delta T_{\mathrm{E}}^{1-2} \\ \delta T_{\mathrm{E}}^{2-3} \\ \delta T_{\mathrm{E}}^{1-3} \\ \vdots \\ d T_{\mathrm{N-E}}^{1} \\ d T_{\mathrm{N-E}}^{2} \\ d T_{\mathrm{N-E}}^{3} \\ \vdots \\ d T_{\mathrm{N-E}}^{M} \\ 0
\end{pmatrix}
\tag{C1}
$$

This problem has the classic least-squares solution $\mathbf{m}_{\mathrm{est}} = [\mathbf{G}^{\mathrm{T}}\mathbf{G}]^{-1}\mathbf{G}^{\mathrm{T}}\mathbf{d}$ (Menke 1984). We choose to include a weighting function whereby each datum is weighted by the maximum value of the cross-correlation, $c_{\max}$, of that measurement in order to give more weight to measurements that may be more robust. The weighting matrix is a diagonal matrix of squares of $c_{\max}$ values: $[\mathbf{W}_{\mathrm{d}}]_{i,j} = a_i^2\,\delta_{i,j}$ where $\delta_{i,j}$ is the Kronecker delta. The weighted least-squares solution is then: $\mathbf{m}_{\mathrm{est}} = \left[\mathbf{G}^{\mathrm{T}}\,\mathbf{W}_{\mathrm{d}}\,\mathbf{G}\right]^{-1}\mathbf{G}^{\mathrm{T}}\,\mathbf{W}_{\mathrm{d}}\,\mathbf{d}$ (Menke 1984).

Downloaded from http://gji.oxfordjournals.org/ at Columbia University on June 6, 2016